*J. Fluid Mech.* (1998), *vol.* 377, *pp.* 313–345. Printed in the United Kingdom



# Direct numerical simulations of bubbly flows. Part 1. Low Reynolds number arrays

By ASGHAR ESMAEELI AND GRÉTAR TRYGGVASON

Department of Mechanical Engineering and Applied Mechanics, The University of Michigan, Ann Arbor, MI 48109, USA

(Received 23 January 1996 and in revised form 30 July 1998)

Direct numerical simulations of the motion of two- and three-dimensional buoyant bubbles in periodic domains are presented. The full Navier–Stokes equations are solved by a finite difference/front tracking method that allows a fully deformable interface between the bubbles and the ambient fluid and the inclusion of surface tension. The governing parameters are selected such that the average rise Reynolds number is $O(1)$ and deformations of the bubbles are small. The rise velocity of a regular array of three-dimensional bubbles at different volume fractions agrees relatively well with the prediction of Sangani (1988) for Stokes flow. A regular array of two- and three-dimensional bubbles, however, is an unstable configuration and the breakup, and the subsequent bubble–bubble interactions take place by 'drafting, kissing, and tumbling'. A comparison between a finite Reynolds number two-dimensional simulation with sixteen bubbles and a Stokes flow simulation shows that the finite Reynolds number array breaks up much faster. It is found that a freely evolving array of two-dimensional bubbles rises faster than a regular array and simulations with different numbers of two-dimensional bubbles (1–49) show that the rise velocity increases slowly with the size of the system. Computations of four and eight three-dimensional bubbles per period also show a slight increase in the average rise velocity compared to a regular array. The difference between two- and three-dimensional bubbles is discussed.

## 1. Introduction

Bubbly flows are central to many industrial processes. Heat transfer through boiling is the preferred mode in most power plants and bubble-driven circulation systems are used in metal processing operations such as steel making, ladle metallurgy, and the secondary refining of aluminium and copper. Similarly, many natural processes involve bubbles. Bubbles play a major role in the interactions of the oceans with the atmosphere, for example, and both air bubbles near a free surface and cavitation bubbles are of major importance for detection of submarines in naval applications.

In this paper we present results from direct numerical simulations of a system of a few two- and three-dimensional bubbles (or light drops, since the density is finite) at a low but finite Reynolds numbers, $O(1)$, in an initially quiescent homogeneous flow, modelled by periodic domains. While the bubbles are deformable, the actual deformations are small due to the low Reynolds number. The study has two goals: to compare the evolution of freely evolving bubbles to fixed arrays, and to examine the utility of two-dimensional simulations for the understanding of a fully three-dimensional system. Several authors have used regular arrays to compute the

properties of particle suspensions in Stokes flows (see references later) and while some quantities obviously cannot be obtained, such as the variance of the bubble velocity and the bubble dispersion, other quantities such as the rise velocity and the added mass may perhaps be well approximated by simple regular arrays. Two-dimensional approximations have a long history in fluid mechanics and although it is obvious that there are quantitative differences between two- and three-dimensional flows, it is of interest to understand what aspects of the flow are well reproduced and which are not, since two-dimensional simulations are much easier to conduct.

Generally, bubbly flows consist of a large number of bubbles moving in a highly unsteady manner, and considerable effort has been devoted to the development of engineering models for the mean motion. The construction of such models for bubbly flows follows closely the derivation of the Reynolds-averaged equations for single-phase turbulent flows. The averaging process can lead to different forms of the model equations, depending on how the averaged variables are selected, but the two-fluid model, where separate conservation equations are derived for each phase, is currently the most common one. See Biesheuvel & van Wijngaarden (1984) for the derivation of a system of equations for one-dimensional inviscid flow of spherical bubbles and Drew (1983), Ishii (1987), Drew & Lahey (1993), and Zhang & Prosperetti (1994) for details of the two-fluid model. The averaging is more complex than for single-phase flow due to the presence of the moving phase boundary and the resulting equations contain unknown terms representing the average force of one phase on the other as well as terms that describe momentum transfer due to velocity fluctuations (the Reynolds stresses). Although the mean motion is usually of most interest, the unknown terms depend on the small-scale motion, thus requiring an understanding of the interaction of each bubble with the fluid as well as with each other. For transport of mass and heat, the rate of dispersion of the bubbles and the velocity fluctuations in the liquid are also required.

In general, the forces and thus the relative velocities between the phases have to be taken from empirical correlation. Experimental investigations of homogeneous bubbly flows can be found, for example, in Lance & Bataille (1991), and Mizukami, Parthasarathy & Faeth (1992) examine turbulence generation in homogeneous particle flows. Earlier experimental work is discussed in both papers. Experiments using a homogeneous 'quasi two-dimensional' fluidized bed are described in Singh & Joseph (1995). Ishii & Zuber (1979) have developed empirical correlations for the relative velocity between a dispersed phase and a continuous one, generalizing earlier studies such as those of Richardson & Zaki (1954) and Zuber (1964) for solid particles. However, in the limit of infinite and zero Reynolds numbers, several authors have attempted to derive these relations theoretically. Here, we will discuss briefly investigations in the Stokes flow limit. For a discussion of the high Reynolds number case, see Esmaeeli & Tryggvason (1999). Early work on the sedimentation of particles in Stokes flow is reviewed by Happel & Brenner (1965) and Davis & Acrivos (1985). Batchelor (1972) computed the sedimentation velocity of a random distribution of solid particles by accounting for pair interactions among the particles and found that the relative velocity for dilute suspensions decreased linearly with the volume fraction. Later investigations have extended these results to polydispersed systems (Batchelor 1982; Revay & Higdon 1992), and drops and bubbles (Wacholder 1973; Haber & Hetsroni 1981). For larger concentrations, investigators have generally used the so-called cell models where the effect of a finite volume fraction is accounted for by solving for the motion of a single particle in a finite domain. Various domains have been used, with various boundary conditions on the outer boundary. See Happel &

Brenner (1965) for a review of early work. From a computational point of view, the simplest cell model is a fully periodic domain containing a single bubble. For Stokes flows, Hasimoto (1959), Sangani & Acrivos (1982*a*, *b*), and Zick & Homsy (1982) have determined the average drag on solid cylinders and spheres, both analytically as well as numerically. Sangani & Acrivos (1983) extended the result to bubbles and Sangani (1988) generalized the results to arbitrary viscosity ratios. For dilute flows, the cell models predict that the relative velocity decreases as the cubic root of the volume fraction and that the drag is lower than that of randomly oriented arrays. Experiments generally show results that fall in between the predictions for random and regular arrays. See Davis & Acrivos (1985) for a review.

In addition to the determination of the appropriate form of the velocity versus volume fraction relation, other aspects of the evolution of a large number of particles in Stokes flow have been examined. Caflisch & Luke (1985) showed that for a random collection of spherical particles the fluctuations of the particle velocity (and hence the fluid velocity) depend on the size of the system. This prompted Koch & Shaqfeh (1991) to develop a theory predicting a non-uniform particle distribution that leads to screening of long-range interactions and thus finite variance of the particle velocity for infinitely large systems. Numerical simulations of freely evolving particles have allowed a more detailed study of the evolution. Brady and collaborators (see Brady & Bossis 1988, for example) used a multipole method to examine the behaviour of a small periodic system and Ladd (1993) extended the results to larger systems (up to 108 particles). He found that the sedimentation velocity depended on the number of particles and the number of moments used to represent each particle. He extrapolated his results to infinitely large systems and found good agreement with the Richardson–Zaki correlation. Ladd examined the microstructure of the suspension and found that there was an excess of particles near contact but an overall deficit of particles within the shell of nearest neighbours, compared with a completely random distribution of particles. In addition, he found that there was a very weak preference for horizontal orientation of particle pairs. While some of his findings had some similarity to the Koch & Shaqfeh (1991) theory, the details were different. Ladd's computations predicted significantly less horizontal excess than the theory and, unlike the theory, the computations showed that the variance of the particle velocity increased with the size of the system, in agreement with the predictions of Caflisch & Luke (1985). To further examine the effect of the size of the system, Ladd has recently conducted simulations of systems with up to 32 000 particles using a lattice-Boltzmann method (Ladd 1997). These new results confirm the divergence of the velocity variance with the system size. The fact that experiments (Nicolai & Guazzelli 1995) seem to show that the variance is independent of the system size remains unexplained. Comparable simulations for bubbles have not been done, to our knowledge.

Although we deal with finite Reynolds numbers here, we expect some similarity with Stokes flow, since the Reynolds number is low. However, the presence of inertia adds fundamentally new effects. At finite inertia, spherical particles can experience lift forces if they move in a non-uniform flow and a particle pair in a quiescent flow will change its relative position even if no other particles are present. The lift force has been used by Koch (1993) to predict that there is a deficit of bubbles in the wake of other bubbles at $O(1)$ Reynolds numbers and that this inhomogeneity in the bubble distribution leads to a finite velocity variance.

The use of direct numerical simulations of the full time-dependent Navier–Stokes equations has become a standard tool in turbulence research. Although the need for a similar approach is widely recognized by multiphase flow researchers, the

computational difficulties in dealing with the unsteady phase boundary have limited such direct simulations to very simple systems. In the limit of high and low Reynolds numbers, it is sometimes possible to simplify the flow description considerably by either ignoring inertia completely (Stokes flow) or by assuming that viscous effects are small and that the flow is irrotational. Most success has been achieved with rigid, spherical particles. In both limits, it is possible to reduce the governing equations to a system of coupled ordinary differential equations for the particle positions. For Stokes flow the simulations of Brady and collaborators and Ladd have had a major impact on the current understanding of such flows, as reviewed above. For potential flows, Sangani & Didwania (1993) and Smereka (1993) simulated the motion of spherical bubbles in a periodic box (both with and without viscous drag) and observed that the bubbles tended to form horizontal clusters, when the variance of the bubble velocities was small. When they include a drag force, the variance was always found to diminish with time.

For both Stokes and potential flows, problems with deformable boundaries can be simulated using boundary integral techniques. For Stokes flow, Zhou & Pozrikidis (1993, 1994) have simulated the unsteady motion of twelve two-dimensional drops both in a shear flow and in a channel where the flow is driven by a pressure gradient. Fully three-dimensional boundary integral computations of the interactions of two drops have been presented by Manga & Stone (1993), Kennedy, Pozrikidis & Skalak (1994) have examined the deformation of a single drop in a shear flow, and Loewenberg & Hinch (1996) have computed the motion of twelve drops in a periodic channel. Chahine and collaborators (see Chahine 1994, for example) have computed the interactions of a few inviscid cavitation bubbles.

For intermediate Reynolds numbers it is necessary to solve the full Navier–Stokes equations. In order to avoid solving for the detailed flow field around each particle, a number of investigators have used point particles in an attempt to simulate dilute multiphase flows. The particles are advected in a constant-density fluid by integrating Newton's second law for each particle. The flow itself is simulated by standard methods (often spectral methods). In some cases the influence of the particles on the flow are neglected, in other cases the force on the fluid from the particles is added to the Navier–Stokes equations. Although this approach is often referred to as 'direct simulations' by its practitioners, the forces on each particle are related to its motion and the fluid velocity by semi-empirical relations and this method is only applicable to dilute flows where there are no direct bubble–bubble interactions. See Wang & Maxey (1993) and Elghobashi & Truesdell (1993), for example. For recent progress in understanding the forces on a single bubble the reader is referred to Magnaudet (1997).

For finite Reynolds numbers and particles of a finite size, a number of authors have simulated the motion of a single particle. We mention only the seminal work of Ryskin & Leal (1984), who computed the steady-state shape of axisymmetric bubbles, and the more recent three-dimensional simulations of the unsteady motion of deformable bubbles by Takagi & Matsumoto (1994) and Miyata (1996). For many bubbles and particles, the literature is rather limited. Feng, Hu & Joseph (1994, 1995) simulated the two-dimensional, unsteady motion of two rigid particles, Unverdi & Tryggvason (1992*a*, *b*) computed the interactions of two, two- and three-dimensional bubbles, and Tomiyama *et al.* (1994) showed a computation of four bubbles. Esmaeeli & Tryggvason (1996) simulated the unsteady motion of a few hundred two-dimensional bubbles, and Hu (1996) computed the motion of a few hundred two-dimensional rigid particles. Fully three-dimensional simulations of a hundred rigid particles have been

presented by Johnson & Tezduyar (1997). Feng *et al.* (1994) examined the settling of circular and elliptic particles in a vertical channel, showing both steady-state settling at low Reynolds numbers as well as the 'drafting–kissing–tumbling' behaviour identified earlier by Fortes, Joseph & Lundgren (1987) at higher Reynolds numbers. The results of Esmaeeli & Tryggvason (1996) will be discussed later.

The rest of the paper is organized as follows. Section 2 contains the formulation of the problem, a discussion of the governing non-dimensional parameters, and a short description of the numerical method. In § 3 we present our results. Two-dimensional simulations are discussed in §§ 3.1 and 3.2. Three-dimensional results are presented in § 3.3 and in § 3.4 the effect of the volume fraction, for both the two- and the three-dimensional results, is discussed. Section 4 contains conclusions.

## 2. Formulation and numerical method

### 2.1. *Governing equations*

The Navier–Stokes equations govern the fluid motion both inside and outside the bubbles. In simulating the motion of two immiscible fluids, surface tension at the fluid interface must be accounted for and incorporating it into the Navier–Stokes equations results in a single vector equation for the whole flow field. In conservative form

$$\frac{\partial \rho \boldsymbol{u}}{\partial t} + \nabla \cdot \rho \boldsymbol{u}\boldsymbol{u} = -\nabla p + (\rho_0 - \rho)\boldsymbol{g} + \nabla \cdot \mu(\nabla \boldsymbol{u} + \nabla \boldsymbol{u}^T) + \sigma \int_F \kappa' \boldsymbol{n}' \delta^\beta(\boldsymbol{x} - \boldsymbol{x}')\, \mathrm{d}A'. \quad (2.1)$$

Here, $\boldsymbol{u}$ is the velocity, $p$ is the pressure, $\rho$ and $\mu$ are the discontinuous density and viscosity fields, respectively, $\sigma$ is the surface tension coefficient, and $\boldsymbol{g}$ is the gravity acceleration. Surface forces are added at the interface between the bubbles and the ambient fluid. $\delta^\beta$ is a two- or three-dimensional delta function constructed by repeated multiplication of one-dimensional delta functions. The dimension is denoted by $\beta = 2$ or 3. $\kappa$ is the curvature for two-dimensional flows and twice the mean curvature for three-dimensional flows. $\boldsymbol{n}$ is a unit vector normal to the bubble surface pointing into the bubble. Formally, the integral is over the entire front, thereby adding the delta functions together to create a force that is concentrated at the interface but smooth along the surface of the bubbles. $\boldsymbol{x}$ is the point at which the equation is evaluated and $\boldsymbol{x}'$ is the position of the front. Since the delta function has a finite support, integrating over the entire front for every point in the flow is neither practical nor necessary and in the numerical code we use a different, but equivalent expression for the surface tension. This will be discussed shortly.

Both the bubbles and the ambient fluid are taken to be incompressible, so the velocity field is divergence free:

$$\nabla \cdot \boldsymbol{u} = 0. \quad (2.2)$$

When combined with the momentum equation, (2.2) leads to a non-separable elliptic equation for the pressure. We also have equations of state for the density and the viscosity:

$$\frac{\mathrm{D}\rho}{\mathrm{D}t} = 0; \quad \frac{\mathrm{D}\mu}{\mathrm{D}t} = 0. \quad (2.3)$$

Here, $\mathrm{D}/\mathrm{D}t$ is the material derivative and theses equations simply state that the density and the viscosity of each fluid remain constant.

These equation implicitly enforce the proper stress conditions at the fluid interface. If we integrate the normal component of (2.1) over a small volume containing the

interface, most of the terms go to zero as we shrink the integration volume, and in the limit of infinitesimal volume we end up with

$$[-p\boldsymbol{I} + \mu(\nabla \boldsymbol{u} + \nabla \boldsymbol{u}^T)] \cdot \boldsymbol{n} = \sigma\kappa\boldsymbol{n}, \tag{2.4}$$

where the brackets denote the jump across the interface. This is, of course, the usual statement of continuity of stresses at a fluid boundary, showing that the normal stresses are balanced by surface tension. Integrating the tangential component shows that the tangential stresses are continuous and integrating the mass conservation equation (2.2) across the interface shows that the continuity of the normal velocities is also satisfied.

For domains that are periodic in the direction of gravity, we need to impose additional constraints to prevent uniform downward acceleration of the whole flow field. Here, we add a body force $\rho_0 \boldsymbol{g}$, where $\rho_0$ is the average density, to the equations for this purpose. This ensures that the net flux of vertical momentum through the computational domain is zero. If the bubbles were completely massless, this would be equivalent to imposing no net throughflow of liquid, as in a container full of liquid with bubbles injected at the bottom and leaving at the top. Here, however, a small net throughflow sometimes develops since mass is not conserved exactly. All our results have been corrected by subtracting this throughflow.

The rise of a single buoyant bubble is governed by four non-dimensional numbers. Two are the ratios of the bubble density and viscosity to the ones of the outer fluid: $\gamma = \rho_b/\rho_f$ and $\lambda = \mu_b/\mu_f$. Here, the subscript $f$ denotes the ambient fluid and $b$ stands for the fluid inside the bubbles. The remaining two numbers can be selected in a number of ways. If we pick the density of the ambient fluid, $\rho_f$, the effective diameter of the bubble, $d_e$, and the gravity acceleration, $g$, to make the other variables dimensionless we obtain

$$N = \frac{\rho_f^2 d_e^3 g}{\mu_f^2}; \quad Eo = \frac{\rho_f g d_e^2}{\sigma}. \tag{2.5}$$

The first number is sometimes called the Galileo or the Archimedes number (see Clift, Grace & Weber 1978) and is a Reynolds number squared based on the velocity scale $(d_e g)^{1/2}$, thus measuring the relative importance of buoyancy and viscous forces. The second one is usually called the Eötvös number and is the ratio of buoyancy to surface tension. In the chemical engineering literature, $N$ is often replaced by the so-called Morton number, $M = g\mu_f^4/\rho_f\sigma^3 = Eo^3/N^2$, which is a constant for a given fluid if the gravity acceleration is constant. While it is obviously convenient to work with a number that is constant for a given liquid, it is somewhat awkward for identifying the relative importance of the governing physical effects. In particular, when bubbles are small and surface tension is high, the bubbles remain spherical and the dynamics is independent of the surface tension (for clean bubbles). When using $N$ and $Eo$ it is clear that when $Eo \to 0$, the motion of the bubbles is a function of $N$ alone. This is not the case if $Eo$ and $M$ are used. For bubble clouds where many bubbles rise together, the volume fraction $\alpha$, defined as the ratio of the volume (area in two dimensions) of the bubbles to the total volume (area), must also be specified.

The behaviour of a single, clean, buoyant bubble is reasonably well understood (Clift *et al.* 1978). For low $Eo$, bubbles remain spherical and their rise velocity, usually expressed as a rise Reynolds number, is steady and a function of $N$ only. For high $Eo$, the bubbles remain spherical at low $N$, but at higher $N$ they become ellipsoids as $Eo$ increases, and eventually 'spherical cap bubbles' at very high $Eo$. For moderate $N$,

the ellipsoidal bubbles have a steady-state rise velocity, but at higher $N$ their motion is unsteady, following a zigzag or a helical path. At high $N$, the wake of a spherical cap bubble is usually turbulent.

### 2.2. *Numerical method*

The integral form of the Navier–Stokes equations is applicable to any flow, including flows with discontinuous material properties. It is well known that if the conservative differential form (2.1) is discretized, the resulting discrete scheme is also a discrete approximation to the integral form and therefore, in principle, applicable to any flow. Several numerical methods take advantage of this fact, including the marker-and-cell (MAC) method for multifluid flow (see e.g. Harlow & Welch 1965), the volume-of-fluid (VOF) method (Hirt & Nichols 1981), the recent level set method of Osher and collaborators (see e.g. Sussman, Smereka & Osher 1994), and a whole host of methods for the compressible Euler equations. Generally, dealing with a fluid interface in this way is called front capturing, to distinguish it from front tracking where the governing equations are solved separately for each fluid and the interface conditions explicitly enforced at the interface. Several versions of such tracking methods exists, see, for example, Ryskin & Leal (1984) and Glimm (1991), for two entirely different approaches. Traditionally, there have been two main difficulties with front capturing. The first, and the more serious one, is the difficulty in maintaining a sharp boundary between the fluids. The different ways of dealing with this are what distinguish between the various front capturing methods. The second difficulty has been the accurate computation of surface tension. Recently, considerable progress has been made in overcoming the second problem (Brackbill, Kothe & Zemach 1992; Lafaurie *et al.* 1994), but advecting the material interface has not been completely solved yet, although level set techniques and high-order VOF methods hold considerable promise.

Our technique is best described as a hybrid between front capturing and front tracking. We work with one set of the governing equations for both fluids, but introduce additional computational elements to represent the front. The front is resolved by discrete computational points that are moved by interpolating their velocities from the grid. These points are connected by triangular elements (lines in two dimensions) to form a front that is used to keep the density and viscosity stratification sharp and to calculate surface tension. At each time step information must be passed between the front and the stationary grid. This is done by a method similar to the one discussed by Unverdi & Tryggvason (1992*a*), where the density jump is distributed to the grid points next to the front and a smooth density field that changes from one density to the other over two to three grid spaces generated by the solution of a Poisson equation. While this replaces the sharp interface by a slightly smoother grid interface, numerical diffusion of the density and the viscosity fields is eliminated, since the grid field is reconstructed at each step.

For the simulations presented here, the method developed by Unverdi & Tryggvason had to be modified to improve its accuracy for long time simulations. In the original method, surface irregularities would occasionally arise at late times due to the technique used to compute surface tension. While these could be easily smoothed out, smoothing affected volume conservation. A new method, that has proven to be both accurate and robust, was therefore developed. The method is based on the fact that it is possible to convert the surface integral of the curvature into a contour integral over the edges of the element (see Weatherburn 1927) and compute the total

surface force on each element (which is what is actually required) directly by

$$\Delta \boldsymbol{F}_e = \sigma \oint_e \boldsymbol{t} \times \boldsymbol{n}\, \mathrm{d}s. \tag{2.6}$$

The integration is over the boundary of each element representing the front. The tangent and the normal vector ($\boldsymbol{t}$ and $\boldsymbol{n}$) are found by fitting a quadratic surface to the vertices of each triangular element and the three additional vertices of the adjacent elements and performing the appropriate differentiation. To ensure that the vectors on a common edge of two elements are the same, the vectors from adjacent elements are averaged. By computing surface forces in this way, we ensure that the total force on a closed surface is zero. This is important for long time simulations since even small errors can lead to a net force that moves the bubbles in an unphysical way. The two-dimensional form is

$$\Delta \boldsymbol{F}_e = \sigma \int_{\Delta s} \frac{\partial \boldsymbol{t}}{\partial s} \mathrm{d}s = \sigma(\boldsymbol{t}_2 - \boldsymbol{t}_1), \tag{2.7}$$

where the integration is over each element, $\boldsymbol{t}$ is a tangent vector computed by fitting a polynomial to the end points of each element, and $s$ is an arclength coordinate. Once the surface force of each element has been computed, it is distributed to the nearest points of the underlying fixed grid, in the same manner as the density jump, and added to the right-hand side of the momentum equations.

As the bubbles move and deform, it is necessary to add and delete points at the front and to modify the connectivity of the points to keep the front elements of approximately equal size and as 'well-shaped' as possible. This operation is performed at every time step, and generally affects only a small number of the front elements at each time. The details are described in Unverdi & Tryggvason (1992*a*). Although we have computed flows with a change in topology (Esmaeeli 1995), in the simulations presented in this paper we do not allow the bubbles to coalesce. The interest here is in averages over statistically steady-state motions of a fixed number of bubbles of a given size, and we have elected to leave out the added complications of coalescence for the time being.

The Navier–Stokes solver is relatively conventional. We use a fixed, regular, staggered grid and discretize the momentum equations using a conservative, second-order centred difference scheme for the spatial variables and an explicit second-order time integration method. The pressure equation, which is non-separable due to the difference in density between the bubbles and the ambient fluid, is solved by a multigrid iteration (MUDPACK, see Adams 1989). The front tracking method is easily used in conjunction with other Navier–Stokes solvers. In Tryggvason & Unverdi (1990), for example, the vorticity–stream function form of the fluid equations, on a regular grid, was used.

The method and the code has been tested in various ways. We have, for example:

(i) Computed the oscillation frequency of two-dimensional drops and compared it with analytical solutions from Lamb (1932). For the resolution used here, the results are generally within a few percent of the analytical one. Specifically, for a two-dimensional drop of diameter 0.4 in a 1 by 1 computational domain, with density 20 times higher than the ambient fluid, we find that the oscillation period is 9.3% longer than the theoretical value on a $32^2$ grid, 3.4% longer on a $64^2$ grid, and 1.9% longer on a $128^2$ grid, when the initial amplitude is 5% of the drop radius.

(ii) Compared the rise velocity of regular arrays of low Reynolds number viscous drops with the result of Sangani (1988) for drops in a Stokes flow. For density and

viscosity ratios of 1/10 and $\alpha = 0.0335$, Sangani's Reynolds number is 0.0599. Our Reynolds number is 0.051 for a grid resolution of $34^3$ and 0.061 58 for a $66^3$ grid. This gives a relative error of 8.9% and 2.57%, respectively. At $\alpha = 0.1256$, Sangani's Reynolds number is 0.0394 and our Reynolds number is 0.0371 at grid resolution of $34^3$ and 0.0395 at grid resolution of $66^3$. This gives a relative error of 4.99% and 0.445%, respectively.

(iii) Examined the motion of a two-dimensional strip of light fluid in a vertical channel. The fluid falls downward until the gravity force is balanced by viscous shear and a steady-state downflow is established. The channel is one unit wide, and the strip is 0.4 unit thick, located in the middle of the channel. Other parameters are taken to be the same as for the bubble simulation in the next section. This problem has an analytical solution and we find that the computed volume flow rate in the channel at steady state is 4.8% of the theoretical value for 32 grid points across the channel, 2.5% for 64 points, and 0.8% for 128 points. The convergence rate for the transient response is comparable.

(iv) Used an axisymmetric version of the code to compute the rise of a low Reynolds number bubble in a pipe and compared the results with theoretical predictions. For a bubble rising with Reynolds number 0.163, resolved by twenty grid points per radius we find that this rise Reynolds number is 1.8% lower than what is predicted analytically by assuming Stokes flow.

(v) Using the same axisymmetric code we have compared our results with one case computed by Ryskin & Leal (1984). For $Re = 20$ and $We = 12$, they found $C_d = 0.33$ on the grid that they used for most of their computations. We found $Eo$ and $M$ from these values and followed the motion of a bubble, using a very large domain and about 25 grid points per bubble radius, until it reached a steady-state velocity. This velocity was within 2% of Ryskin & Leal's prediction (see Jan 1993).

Although the axisymmetric code is not the same as the one used here, the method is the same, and the axisymmetric and the three-dimensional codes have been compared to each other. We have also conducted extensive grid refinement studies to assess the accuracy of the simulations presented here. Some of those will be discussed in the results section.

Run times depended strongly on the volume fraction and the number of bubbles simulated. The three-dimensional simulation of eight bubbles at $\alpha = 0.0654$ (middle frame in figure 8*b*) was run for 68 673 time steps and each step took about 110 s on a Convex SPP-1600 computer. The two-dimensional simulation of 16 bubbles in figure 2 was run for 82920 time steps and each step took about 5 s on the same platform. Computational requirements for the other simulations were comparable.

## 3. Results

The simulations presented here are all done in a fully periodic domain so that the bubble configuration in each cell is repeated indefinitely in each direction. The governing parameters are selected in such a way that the rise Reynolds number is low and the bubbles remain nearly undeformed. In terms of the non-dimensional numbers introduced in the preceding section, we set

$$Eo = 1.0; \quad N = 1000^{1/2}\ (M = 10^{-3}); \quad \gamma = 0.05; \quad \lambda = 0.05.$$

These values of the non-dimensional parameters can, for example, be realized using air bubbles of diameter 1.9 mm in standard engine oil (taking $\sigma = 0.03$ N m$^{-1}$, $\rho = 880$ kg m$^{-3}$, and $\mu = 0.21$ N s m$^{-2}$), with the exception that the density and

viscosity ratios would be lower. Figure 2.5 in Clift *et al.* (1978) gives a rise Reynolds number of about 1.6 for these parameters for a single three-dimensional bubble in an unbounded fluid. Here, the volume fraction is finite and we generally expect the bubbles to rise slower. We also use finite density and viscosity ratios, but extensive tests with lower ratios of the material properties (down to 1/300) have shown that the effects of the bubble density and viscosity are already small for the values used here, see Esmaeeli (1995). At zero Reynolds numbers, the effect of finite property ratios on the steady state can be computed explicitly and we find that a viscosity ratio of 0.05 leads to a 2.3% reduction in the steady-state velocity compared to a zero viscosity bubble. The reduction in rise velocity due to a finite density ratio is directly proportional to the density difference. The values used here are selected for computational convenience, but similar ratios could be obtained by light oils in liquid metals, for example. While it would be obviously of more relevance to air bubbles in water if the density ratio was lower, we believe that the current values do not lead to a fundamentally different behaviour. We note that a similar problem is encountered in boundary integral computations of drops in Stokes flow where the computational effort increases considerably as the viscosity ratio is increased. For simulations of many drops, Zhou & Pozrikidis (1993, 1994) and Loewenberg & Hinch (1996), for example, thus elected to assume equal viscosities in most of their simulations.

When presenting our results, we non-dimensionalize time by $(d_e/g)^{1/2}$ and length by the bubble diameter $d_e$. Velocities are scaled by $(d_e g)^{1/2}$ with the exception of the rise velocity of the bubbles ($W_b$) which is given as a Reynolds number, $Re = \rho_f d_e W_b/\mu_f$. The velocity in terms of units of $(d_e g)^{1/2}$ can be found by dividing the Reynolds number by $N^{1/2}$.

The bubble velocities reported in the result section are all relative velocities, computed as the volume-averaged velocities of the bubbles minus the volume-average velocity of the whole domain. The liquid has an average throughflow velocity given by $W_f = \alpha W_b/(\alpha - 1)$ and the relative velocity of the bubbles with respect to the liquid is given by $W_r = W_b/(1-\alpha)$. The volume-averaged bubble velocity is equal to the velocity of the bubble centroid.

To compute the bubble volume and its centroid velocity we use the fact that the surface of the bubble is explicitly marked by computational points. This allows us to convert the volume integrals to surface integrals using the divergence theorem. For three-dimensional bubbles, the bubble volume is

$$V_b = \int_{V_b} \mathrm{d}v = \frac{1}{3}\int_{V_b} \nabla\cdot\boldsymbol{r}\,\mathrm{d}v = \frac{1}{3}\oint_{S_b} \boldsymbol{r}\cdot\boldsymbol{n}\,\mathrm{d}s,$$

where $\boldsymbol{r}$ is location of a point on the surface. The centroid is

$$\boldsymbol{r}_c = \frac{1}{V_b}\int_{V_b} \boldsymbol{r}\,\mathrm{d}v = \frac{1}{2V_b}\int_{V_b} \nabla(\boldsymbol{r}\cdot\boldsymbol{r})\,\mathrm{d}v = \frac{1}{2V_b}\oint_{S_b} (\boldsymbol{r}\cdot\boldsymbol{r})\,\boldsymbol{n}\,\mathrm{d}s,$$

and the vertical centroid velocity is found by

$$W_b = \frac{1}{V_b}\int_{V_b} w\mathrm{d}v = \frac{1}{V_b}\int_{V_b} \nabla\cdot(z\boldsymbol{u})\,\mathrm{d}v = \frac{1}{V_b}\oint_{S_b} z\boldsymbol{u}\cdot\boldsymbol{n}\,\mathrm{d}s.$$

The accuracy of computing these quantities in this way has been checked by comparing with direct computations of the volume integrals and the velocity of the centroid has been compared with direct differentiation of the centroid positions.

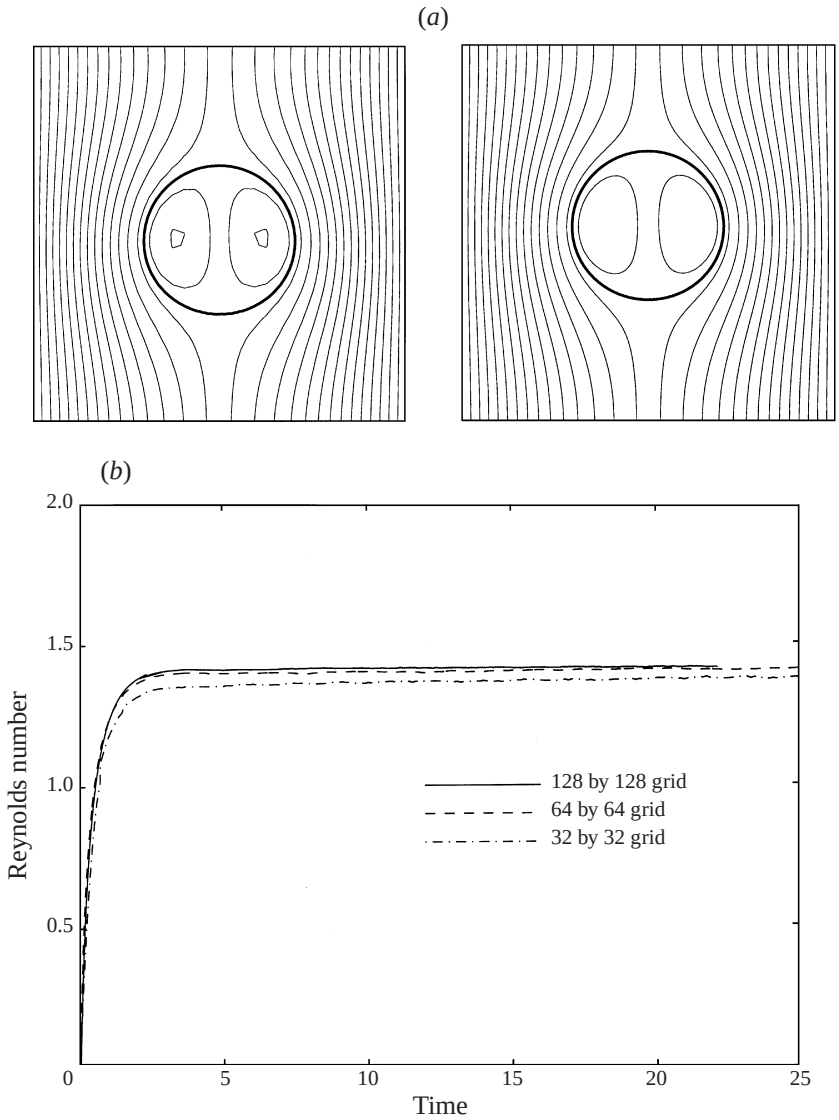


FIGURE 1. (*a*) The rise of a single bubble in a periodic cell for a $32^2$ grid (left frame) and a $64^2$ grid (right frame). The steady-state shape of the bubble and the streamfunction in a reference frame moving with the bubble are shown for both resolutions. The volume fraction is 0.1256. (*b*) The rise Reynolds number for the simulations in (*a*). The initial unsteady motion is well resolved by both grids, but the steady-state rise velocity of the coarsely resolved bubble is about 2.4% lower. Results for a $128 \times 128$ grid simulation are also included and show that the $64 \times 64$ grid results are essentially fully converged.

### 3.1. *The evolution of two-dimensional arrays*

We start by examining the behaviour of a single buoyant bubble in a unit cell. The steady-state shape of the bubble and the stream function in a frame moving with the bubble is shown in figure 1(*a*). In the simulation the domain size is 1, the initial bubble diameter is 0.4, gravity is set to 1, and the fluid density and viscosity are 25 and 1.12468, respectively. The surface tension coefficient is 4.0. This gives

the non-dimensional parameters listed above and a volume fraction of $\alpha = 0.1256$. Results from a run on a $32^2$ grid are shown on the left and from a $64^2$ grid on the right. The rise velocity of the centroid of the bubble, for both resolutions, is plotted in figure 1(*b*). Obviously, there is little difference (2.4%), suggesting that the lower resolution will resolve the motion fairly well. We have also included the result from a computation on a $128^2$ grid to show that the $64^2$ grid results are essentially fully converged. Although the finite difference method is conservative, the front tracking part is not. Nevertheless, mass is well conserved and at the end of the run, after the bubbles have risen over 20 bubble diameters, the area of the bubble on the $32^2$ grid has increased by about 2%, about 0.5% for the $64^2$ grid, and 0.26% for $128^2$ run.

The single bubble in a periodic cell in figure 1 is the simplest cell model that we could use to estimate the properties of a multiphase flow. To examine whether such a regular array is a stable configuration we have run a number of simulations where we put together several single bubble cells, but perturb the initial bubble positions slightly. The results show, in all cases, that a regular array is an unstable arrangement that quickly breaks up. A few frames from one such simulation of 16 bubbles, carried out far beyond the initial breakup, are shown in figure 2. The physical parameters and the volume fraction are the same as in figure 1 and the doubly periodic computational domain is resolved by a $194^2$ grid. This gives a resolution of $48^2$ grid points per unit cell (and about 20 points per bubble diameter) which is between the two resolutions used in figure 1. The bubbles and the stream function (twenty equispaced contours) in a stationary frame are shown at equispaced times noted in the caption. The initial condition (top left-hand corner) is a slightly perturbed regular array, where the bubbles are placed in four columns and four rows. To make it easier to identify how the bubbles move, one row is coloured black. Initially, each column rises relatively undisturbed, but then the bubbles in some of the columns start to pair. As the bubbles collide, they tumble, and the bubble at the back catches up with the one in front. As this process is taking place, the columns become unstable with respect to each other and at later stages it is not possible to identify any particular relation between the instantaneous bubble configuration and the initial condition. The bubbles, however, continue to be drawn into the wake of the ones in front, collide, tumble and move apart. This is, of course, the 'drafting, kissing, and tumbling' described by Joseph *et al.* (1987) for solid particles: for two bubbles rising in tandem, the lower one is in the wake of the one in front and is shielded from the oncoming fluid. It therefore experiences less drag but the same buoyancy force, and moves faster than the one in front. An in-line configuration of two touching bubbles is inherently unstable, and the bubbles 'tumble' whereby the bottom one catches up with the top one. At the end of the tumbling the bubbles move apart. Subsequent frames show several such collisions, in some cases involving three bubbles. Although the clusters of bubbles generated by such collisions are transient and break up rapidly, figure 2 shows that at any given time there is usually one or more cluster present and the bubble distribution is very non-uniform.

To examine in more detail how the bubbles move, we plot the paths of the individual bubbles in figure 3(*a*). The boxes outlined by dotted lines correspond to the periodic computational domains. The bubbles all start in the same periodic box, but at the end of the run (when the centroid has risen more than five periods) the bubbles are spread over more than three periods in the vertical direction and about two periods in the horizontal direction. The sharp turns (or kinks) in the path correspond to bubble collisions due to 'drafting, kissing, and tumbling' (this is even more apparent in computer animations of the results). Two bubbles in Stokes flow rise with equal velocity and can only change their positions if they are influenced by a third bubble.

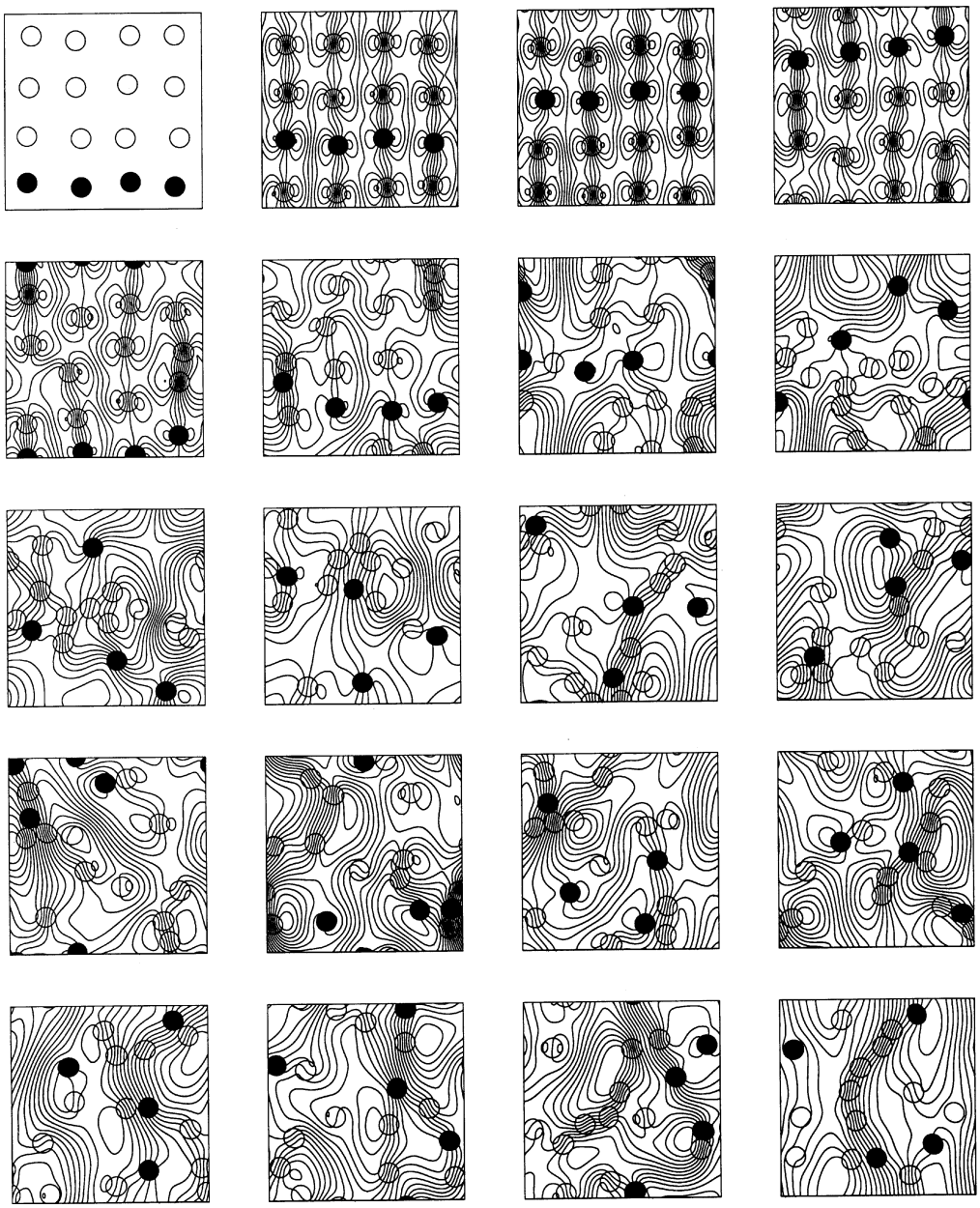

FIGURE 2. Several frames showing 16 bubbles rising in a doubly periodic box. Time proceeds from the left to the right and the top to the bottom. The bubbles and the streamfunction in a stationary frame of reference are shown at time 0 and then every 7.9 time units. The initial conditions (upper left corner) are a regular array, perturbed slightly, and the volume fraction is 0.1256. One row is coloured black to make visualization easier.

We therefore expect that the motion seen here is quite different from Stokes flow. To examine that, we have conducted one Stokes flow simulation. Since our code is explicit in time, this simulation was done by eliminating the advection terms and evolving the viscous terms to steady state in 'pseudo-time' at each 'real' time step. This is a relatively inefficient way of computing the evolution but required minimum changes

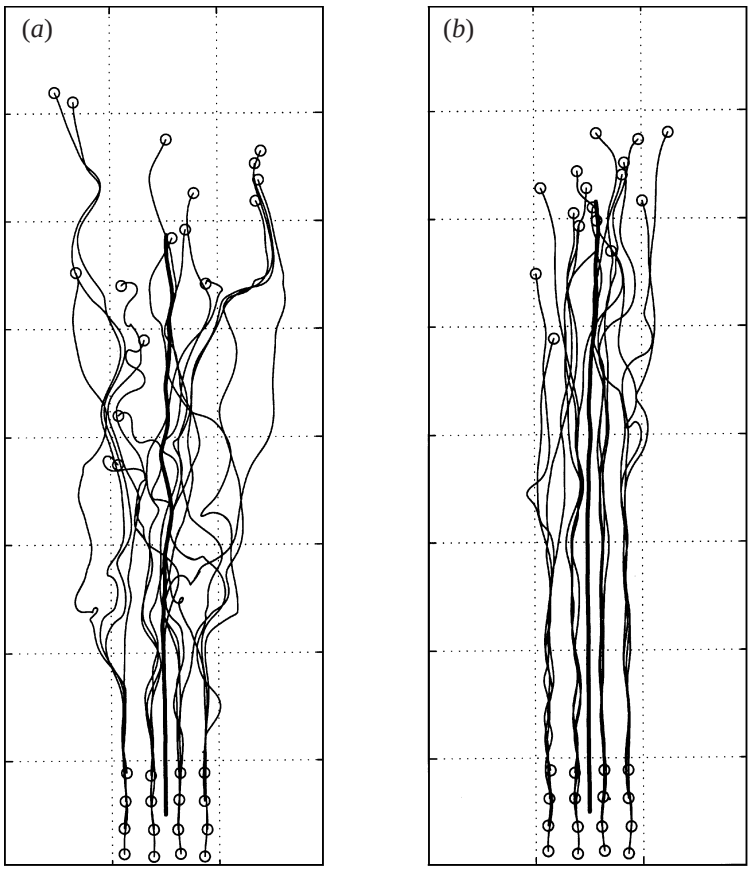


FIGURE 3. The path of the individual bubbles in the simulation in figure 2 is shown on the left (*a*) and the path of bubbles computed by neglecting all inertial effects (Stokes flow) is shown on the right (*b*). The bubbles originally in the computed period are followed as they rise through the other periods. The horizontal and vertical dashed lines mark the boundaries between successive periods. The thick, solid line marks the motion of the centroid of the bubbles. Notice that the small circles that mark the beginning and the end of each path are much smaller than the bubbles.

to our code. The initial position of the bubbles is exactly the same as in figure 2 and the governing parameters are the same as those used in the finite Reynolds number run. Therefore, the rise Reynolds numbers are comparable. The paths of the bubbles for this simulation are shown in figure 3(*b*). While the regular array of bubbles is also an unstable configuration in a Stokes flow, the instability sets in much more slowly and the breakup is delayed. After the breakup, the fluctuations are smaller than those at finite Reynolds number, and the horizontal dispersion of the bubbles is very small.

FIGURE 4. (*a*) The average rise Reynolds number of the bubbles from the simulation in figure 2 versus time. The thick solid line is the ensemble average of the time-averaged Reynolds number from five simulations with different initial conditions and the dashed line is the rise velocity of a regular array (single bubble in a cell) at the same conditions. The rise velocity of Stokes flow bubbles is shown by a dashed-dot line. (*b*) The Reynolds stresses versus time for the simulation in figure 2. The ensemble average of the time-averaged Reynolds stresses from five simulations with different initial conditions are shown by thick lines. (*c*) The asymmetry index, $\langle A \rangle$, versus time for the simulation in figure 2. $\langle A \rangle$ is computed every 50 time steps.

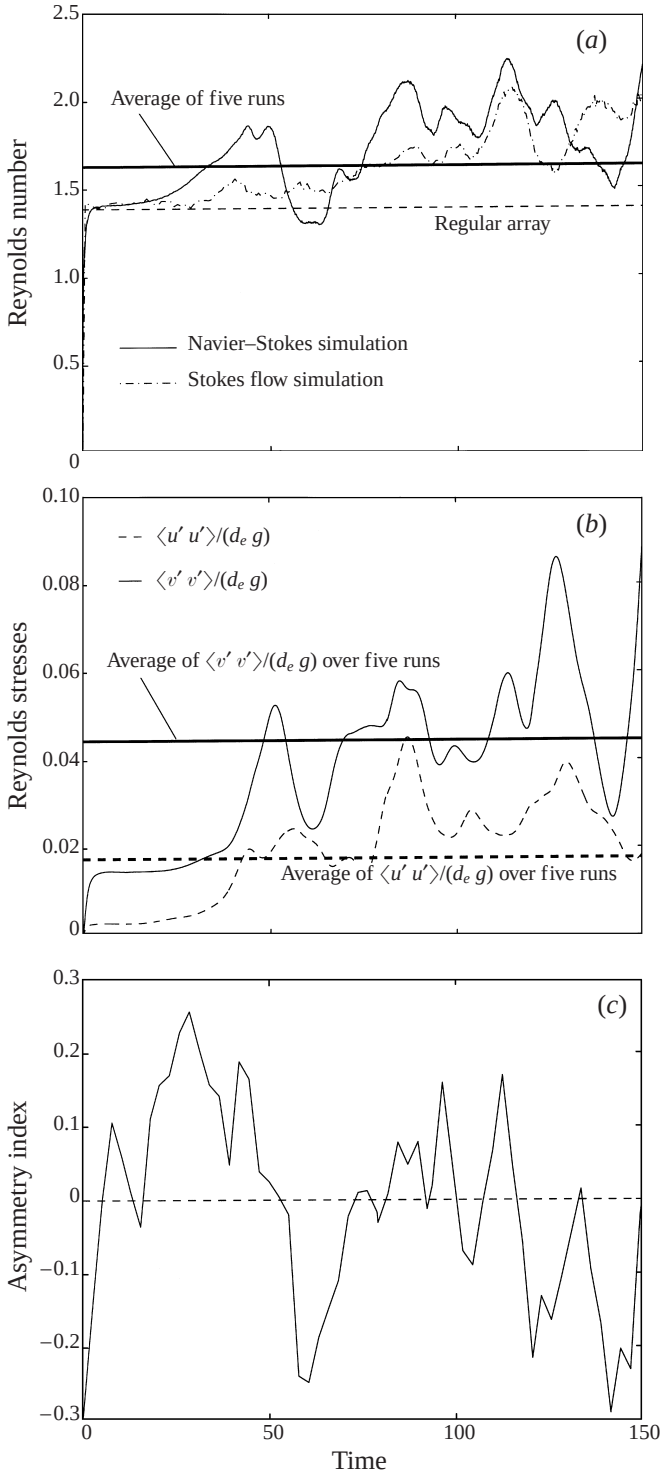


FIGURE 4. For caption see facing page.

| case | *Re* | $\langle v'v' \rangle$ | $\langle u'u' \rangle$ | $\langle u'v' \rangle$ |
|---|---|---|---|---|
| 1 | 1.544 289 5 | 0.034 77 | 0.015 24 | −0.002 855 |
| 2 | 1.640 787 7 | 0.048 92 | 0.014 88 | −0.000 402 |
| 3 | 1.650 057 0 | 0.046 76 | 0.018 78 | −0.001 691 |
| 4 | 1.595 755 9 | 0.040 12 | 0.018 39 | −0.000 100 |
| 5 | 1.711 474 8 | 0.051 76 | 0.020 89 | −0.000 414 |
| Average | 1.628 472 9 | 0.044 47 | 0.017 63 | −0.001 093 |
| SD | 0.055 971 6 | 0.006 18 | 0.002 27 | 0.001 038 |

TABLE 1. Time-averaged Reynolds numbers and Reynolds stresses for five simulations of 16 two-dimensional bubbles at $\alpha = 0.1256$. SD denotes standard deviation.

Figure 4(*a*) shows the rise Reynolds number of the centroids of the bubbles (or the average rise Reynolds number since the bubbles are of the same size) for the run in figure 2. The rise Reynolds number of the Stokes flow run is also plotted. Initially, the Reynolds number increases smoothly to a nearly steady state which is equal to what is predicted for a single bubble in a cell at this volume fraction. Around time 20, when the original columns start to breakup, the velocity increases rapidly, reaches a maximum and then drops off. The velocity subsequently fluctuates, but it is clear that the average is considerably higher than what the single-bubble-in-a-cell model predicts. The Stokes flow run predicts much longer breakup time and smaller fluctuations after breakup. The average rise Reynolds number of the Stokes bubbles increases after the array breaks up, in agreement with theoretical predictions that random arrays rise faster than regular ones (Davis & Acrivos 1985). While the simulation in figure 2 may have reached an approximately statistically steady state, the fluctuations are large and we anticipate the need to average over a long time to obtain fully converged time averages. Furthermore, the initial time where the regular array of bubbles is breaking up is relatively long and should be excluded from the averaging. To generate a larger sample, and to avoid the initial transient, we have conducted five simulations with irregular bubble distributions as initial conditions. Transient clustering takes place nearly immediately and the evolution is similar to the regular array in figure 2 after it breaks up. The average of the centroid rise Reynolds number from these five simulations is shown by a solid horizontal line in figure 4(*a*). It is clear that the average for the freely evolving arrays is slightly more than 20% higher than for the single-bubble-in-a-cell model. The average Reynolds numbers from these simulations, as well as the Reynolds stresses, are also shown in table 1. Generally, the averages from each simulation agree well with each other, suggesting that they are reasonably well converged.

In figure 4(*b*) the Reynolds stresses for the ambient fluid, non-dimensionalized by $d_e g$, are plotted versus time. Again, while the array remains regular the values are nearly constant (and equal to the single-bubble-in-a-cell model), but as the array breaks up the Reynolds stresses increase and start to fluctuate. The vertical stresses $\langle v'v' \rangle$ correlate well with the rise velocity, but for the horizontal stresses, $\langle u'u' \rangle$ the correlation is not as strong. The cross-term (not plotted), $\langle u'v' \rangle$, remains zero while the array is regular, but fluctuates around zero after it breaks up. The average values from the five runs mentioned earlier are shown by horizontal lines.

A close look at the bubble configuration and the streamlines in figure 2 and the 'peaks and valleys' in the rise Reynolds number in figure 4(*a*), allows us to correlate the 'peaks' with flow configurations where there are reasonably well defined upflow streams. The bubbles are usually crowded in those streams, sometimes forming 'chains'

as in the last frame shown, for example. For the valleys the bubble configuration is more irregular, although it is perhaps possible to identify loosely organized horizontal layers at, say, $t = 55.4$ and $t = 63.3$ (last two frames in the second row from the top). To quantify the bubble distribution, we use the pair distribution function, $G(\boldsymbol{r})$. $G$ is the probability of finding a bubble at a given position relative to another bubble and is given by

$$G(\boldsymbol{r}) = \frac{V}{N_b(N_b-1)} \left\langle \sum_{i=1}^{N_b} \sum_{\substack{j=1 \\ j\neq i}}^{N_b} \delta(\boldsymbol{r} - \boldsymbol{r}_{ij}) \right\rangle, \tag{3.1}$$

where $\boldsymbol{r}_{ij}$ is the distance between bubbles $i$ and $j$, $N_b$ is the total number of bubbles and $V$ is the volume (area) of the system. To examine the evolution of the bubble distribution we have computed an 'asymmetry index' of $G$ to determine whether the bubbles are preferentially oriented vertically or horizontally with respect to each other. We define this index as the weighted average of $G$:

$$\langle A \rangle = \frac{1}{V} \int_{d_e}^{2.5d_e} \int_0^{2\pi} G(r,\theta) \cos 2\theta \, \mathrm{d}s, \tag{3.2}$$

where d$s$ is a volume (area) element. If the bubbles are oriented approximately vertically with respect to each other, this quantity is positive and if the bubbles are all in a horizontal layer it is negative. A zero index indicates that there is neither a predominantly horizontal nor vertical orientation. Figure 4($c$) shows this quantity versus time for the run in figure 2. A comparison with the average rise Reynolds number in figure 4($a$) shows a correlation between a positive $\langle A \rangle$ and a higher than average rise Reynolds number and vice versa. In particular, at the early time, when the initially regular array is breaking up by each bubble catching up with the one in front ('drafting'), $\langle A \rangle$ is positive, but once the breakup is completed, it is frequently negative. This will be examined in more detail below.

To examine how the bubbles are distributed with respect to each other on average, we have computed the pair distribution function for five equispaced times for the five 16-bubble runs with random initial distribution of bubbles. The average $G$ is computed over small increments of $\theta$, the angle between $\boldsymbol{r}_{ij}$ and the vertical axis, and over small increments of $r$, the distance from the reference bubble. In figure 5($a$) we plot $\langle G(\theta) \rangle_{\Delta r}$ versus $\theta$ for four intervals between $r/d_e = 1$ and 5. Here, $\Delta\theta = \pi/8$ and $\Delta r = d_e$. The plot shows that for $1 < r/d_e < 2$, $\langle G(\theta) \rangle_{\Delta r}$ has a minimum for $\theta = 0$, but in the intervals with larger radii, it is essentially constant. To condense this information even further, we have also computed the radial dependency of the asymmetry index:

$$A(r) = \int_{\Delta r} \int_0^{2\pi} G(r,\theta) \cos 2\theta \, \mathrm{d}s. \tag{3.3}$$

In figure 5($b$) we plot this quantity for the same increments in $r$ as used in figure 5($a$). The error bars indicate the standard deviation computed from the averages over the five runs. For $r/d_e < 1$, $A$ is zero since there are no bubbles there and for $r/d_e = 1.5$, $A$ is clearly negative. $A$ approaches the zero axis as $r$ increases in agreement with figure 5($a$) which showed that the anisotropy observed for bubbles close to the reference bubble disappears at larger radii.

To find how the bubble orientation correlates with the velocity fluctuations, we have computed the weighted average of $G$ over five bubble radii ($\langle A \rangle$ defined by equation (3.2)), as well as the difference between the instantaneous centroid Reynolds number (averaged over all the bubbles) and the time-averaged Reynolds number for the five

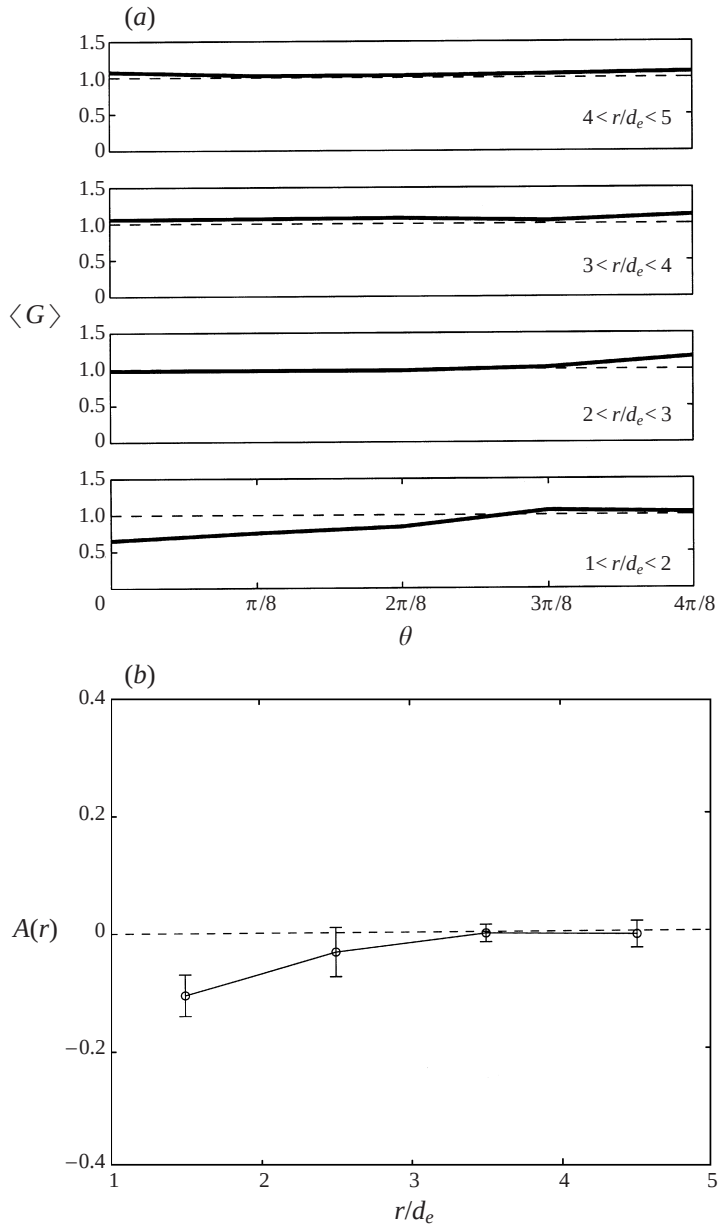


FIGURE 5. (*a*) The bubble pair distribution function for 16 bubbles in a periodic cell, computed by averaging the results from five simulations at five equispaced times. $\langle G \rangle$ is shown versus $\theta$ for four intervals of $\Delta r = d_e$. (*b*) The weighted average of the bubble pair distribution function, $A(r)$, versus radius, averaged over five runs at five equispaced times. The standard deviation of the five run averages is shown by vertical error bars.

16-bubble runs at eighteen equispaced times (excluding time zero). Each such pair is then represented by a circle in figure 6. We have also drawn dashed lines indicating the average values of the asymmetry index (slightly negative) and the Reynolds number fluctuations (zero, by definition). If a positive (negative) value of one quantity always went with a positive (negative) value of the other, all the circles would be in the first (third) quadrant. The correlation is not perfect and we therefore have several points

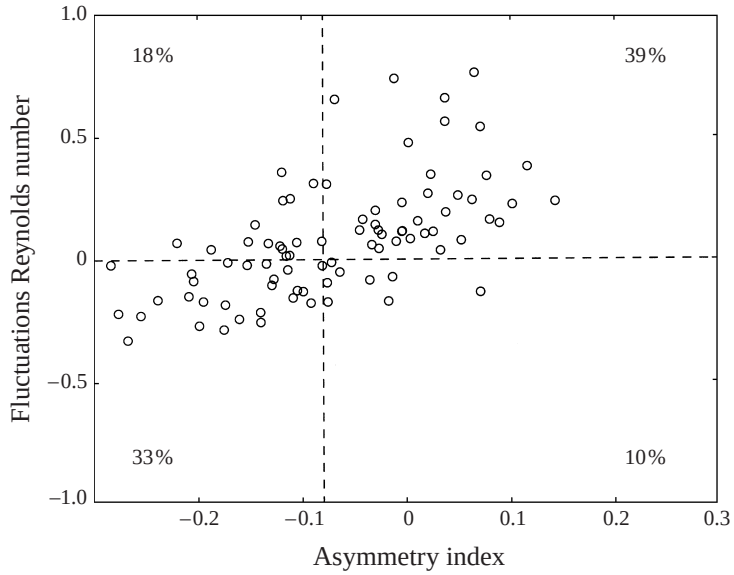


FIGURE 6. The difference between the instantaneous Reynolds number of the bubbles and the time-averaged Reynolds number versus the asymmetry index defined in the text. The points are found at ten equispaced times (excluding time zero) for five runs with different initial conditions. The correlation coefficient between the velocity fluctuations and the asymmetry index is 0.62.

in the second and the fourth quadrant. The percentage of circles in each quadrant is noted on the graph and we see that the first and the third quadrant contains the majority of the points (72%), thus showing that the bubble configuration is correlated with the velocity fluctuations. The negative average value of the asymmetry index suggests a slightly higher probability of finding two bubbles side by side, rather than in tandem, in agreement with the pair distribution in figure 5. We note that in general we would expect a side-by-side configuration to have a higher drag than a tandem configuration, so it is somewhat counterintuitive to find the average bubble Reynolds number of these arrays to be higher than for a regular array. The explanation seems to lie in the generation of well defined streams of several bubbles that move upward together. The lower drag associated with such a cluster, even though the bubbles forming it are side by side (see, for example, figure 2 at $t = 126.6$ – last frame in the third row), seems to offset the increased drag due to bubbles that are side by side.

We have repeated the computations in this section on a coarser $128^2$ grid (versus $194^2$ in figure 2) since the resolution test in figure 1 suggests that this resolution produces reasonably accurate results. Initially, the motion of the bubbles is identical to that in figure 2, but at later time the exact bubble locations are different. This is as we expect: the grid exerts a small random force on the system and these perturbations are different on different grids, even though the physics involved is well represented. Since we are primarily interested in average quantities here, we computed the average rise velocity and the average Reynolds stresses for both runs. On the coarse grid the rise velocity was 5.6% lower. However, the horizontal Reynolds stresses were essentially identical and the vertical Reynolds stresses were 6.4% higher on the coarse grid. These differences in average values are well within what we expect between runs with different initial conditions, since the time over which the averages are computed is relatively short, and for most of the runs in the rest of the paper (including the five runs averaged in figure 4) we have used the coarser resolution.

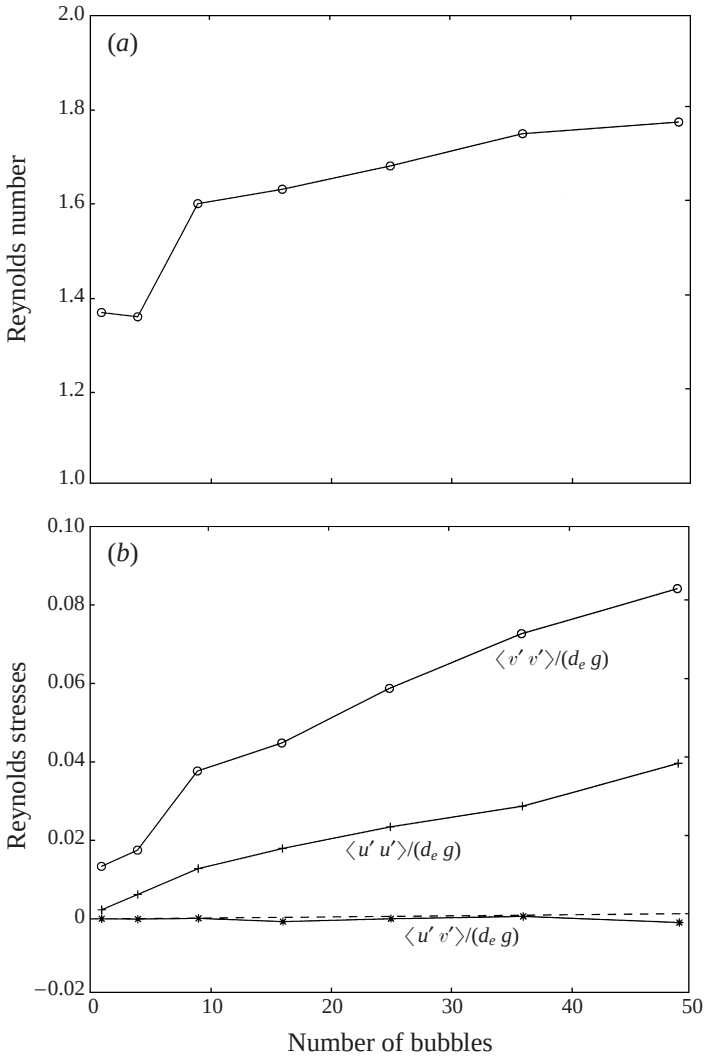


FIGURE 7. (*a*) The effect of the number of bubbles (i.e. system size) on (*a*) the average rise Reynolds number of the bubbles, and (*b*) the ambient Reynolds stresses, in a fully periodic two-dimensional domain. Volume fraction is $\alpha = 0.1256$ and each data point is obtained by averaging over five runs.

### 3.2. *Effect of system size*

Although the averages for the five 16-bubble cases in the last section suggest that the rise velocity and the Reynolds stresses are well converged, the result may not be representative of a very large system. To examine the trend in the averaged quantities as we increase the size of the system, we have done additional simulations using 4, 9, 25, 36, and 49 bubbles, with other parameters kept the same as in the 16-bubble runs. The size of the computational domain is adjusted to maintain the same volume fraction and the grid is selected in such a way that the resolution of each bubble is the same as for the 16-bubble runs. In each case we have simulated the evolution of five different initial conditions up to non-dimensional time of 160. The results from these simulations are summarized in figure 7. Figure 7(*a*) shows the average rise Reynolds number and figure 7(*b*) shows the Reynolds stresses, non-dimensionalized by $d_e g$, as

a function of the number of bubbles used. We also include the results for a single bubble per cell. Obviously, the effect is larger when the number of bubbles is small. The average rise Reynolds number for 16 bubbles is almost 20% higher than for four bubbles, for example, but as the number increases the differences become smaller. However, the results do not approach a constant value. While the bubble Reynolds number increases slowly with the size of the system, the Reynolds stresses increase rapidly and there is no indication that they will level off to a value independent of the size of the system.

To investigate the properties of even larger systems of bubbles, we have done two simulations with 144 and 324 bubbles (each taking several months on a SP1 workstation). These results, which are described in detail in Esmaeeli & Tryggvason (1996), showed that there may be a fundamental problem with the assumption that we can reach a statistically steady-state independent of the size of the system for two-dimensional, finite Reynolds number bubbly flow, due to an inverse energy cascade that continuously feeds work done by the bubbles to larger flow scales. A manifestation of this is seen in figure 2, where it is clear that after the initial regular array has broken up, the largest flow feature is typically half the size of the computational domain or larger. However, the result in figure 7 suggests that average Reynolds number is only weakly dependent on the size of the computational box once we have more than a dozen bubbles or so. We believe that this growth is a finite Reynolds number effect (an inverse energy cascade) and therefore fundamentally different from the divergence of the velocity fluctuations in three-dimensional Stokes flow predicted by Caflisch & Luke (1985) and found numerically by Ladd (1997).

### 3.3. *The evolution of three-dimensional arrays*

While leading to considerable insight into the dynamics of dense bubble clouds, the practical applicability of the results of the previous sections is limited since the bubbles are only two-dimensional. Computations of three-dimensional bubbles of the same complexity are considerably more demanding on computer resources and we have only done simulations with eight bubbles and fewer, so far. Figure 8 shows results from three simulations of four, figure 8(*a*), and eight, figure 8(*b*), bubbles in a fully periodic domain. The eight-bubble runs are done in a cubical domain resolved by a $64^3$ grid and the four-bubble runs are done in a $1 \times 2 \times 2$ domain, resolved by a $32 \times 64 \times 64$ grid. Figure 1 showed that for two-dimensional simulations this resolution led to nearly the same results as a finer grid. The volume fraction is 0.0335, 0.0654, and 0.1256, from left to right. Other parameters are the same as in the two-dimensional computations in the preceding sections. The bubbles are shown at time zero and a few later times, along with the path of each bubble. Here, the bubbles are plotted in a different way than for the two-dimensional results. The computational domain is periodic, so new bubbles enter as the original bubbles leave. For the two-dimensional runs we plot (in figure 2) the bubbles that occupy the original domain, but in figure 8 we follow the original bubbles as they rise through several periods. The original domain and its periodic extensions in the vertical direction are also shown. Initially, the bubbles are placed in a nearly regular array. Like the two-dimensional bubbles they first rise straight upward, but as each bubble reaches the wake of the bubble in front, the array becomes unstable and the initial configuration breaks up. Notice that the dispersion is considerably less than in figures 2 and 3(*a*), and that the paths are smooth, without the sudden change of direction seen in figure 3(*a*), suggesting that collisions are either absent or not as violent as for the two-dimensional bubbles. A close examination of the paths of the bubbles shows that bubble pairs, initially

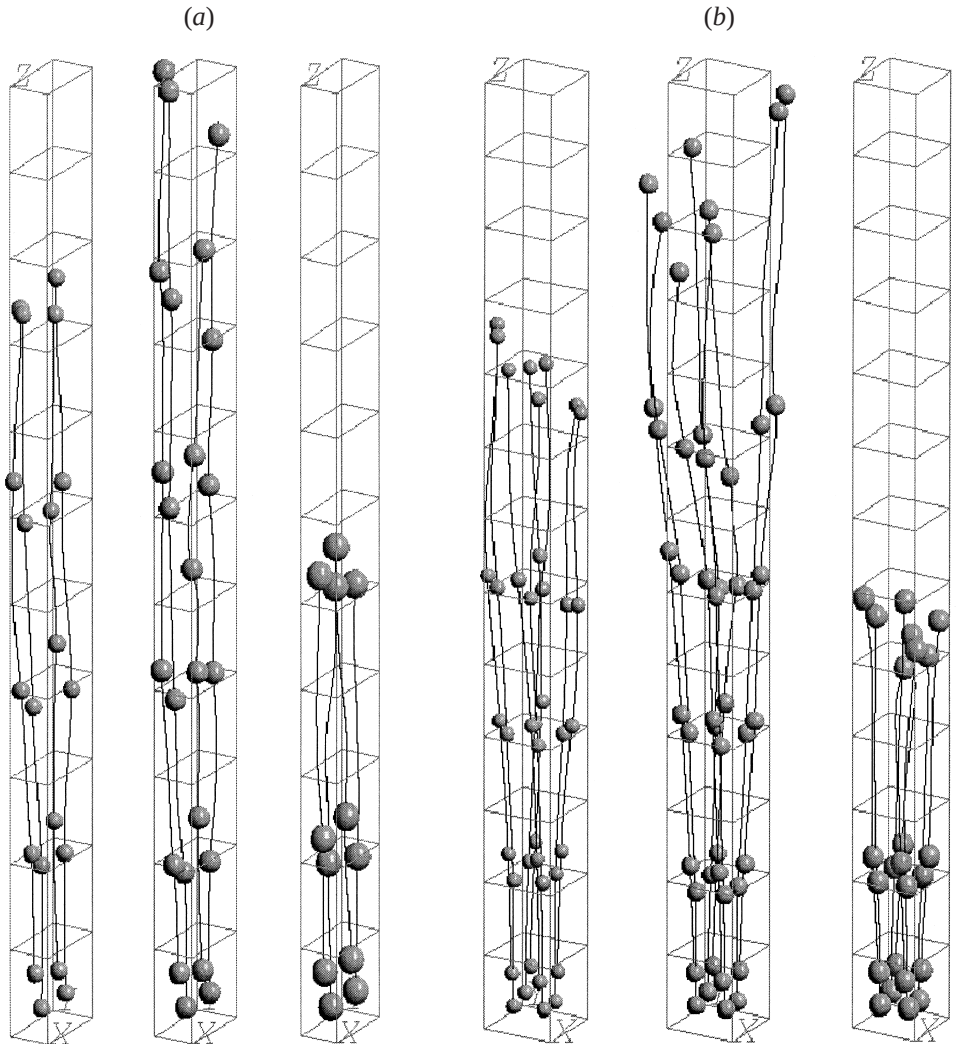


FIGURE 8. Fully three-dimensional simulations of (*a*) four and (*b*) eight bubbles in a periodic cell for volume fractions of 0.0335 (left frame), 0.0654 (middle frame), and 0.1256 (right frame). The bubbles are plotted at selected times and the path of each bubble is shown by a solid line. The outlines of the periodic domains are also shown.

oriented vertically, tend to interact strongly, orient themselves horizontally and rise together. This suggests two-bubble interactions of the same type as seen in the two-dimensional runs. To see how the bubbles affect the flow around them, the streamlines at time 87.0 for the 0.0654 volume fraction run are plotted in figure 9, in a vertical plane through the computational domain. The bubbles occupying the domain at this time are also shown.

The average bubble rise Reynolds number for the three-dimensional computations in figure 8, along with the results for a single bubble in a periodic domain, are plotted versus time in figure 10. While the single bubble approaches a steady state monotonically, the multi-bubble results first show a slight overshoot and then fluctuate as did the two-dimensional multi-bubble runs. The overshoot is a result of somewhat cludgy initial conditions where the regular array was perturbed by moving most of

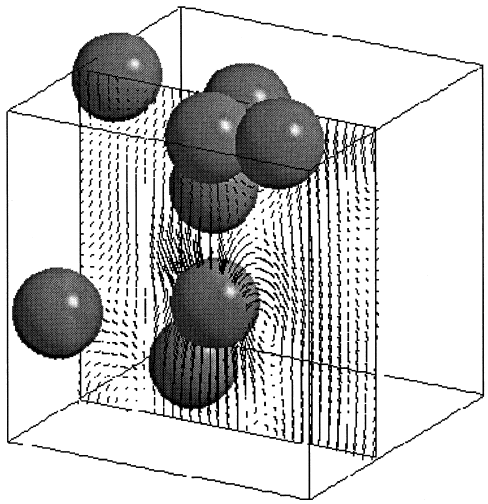

FIGURE 9. The bubbles from the $\alpha = 0.0654$ run in figure 8($b$) and the velocity field in a plane through the computational domain at $t = 87.0$.

the bubbles closer to the centre of the computational domain (to force the bubbles that were in the original domain to interact more strongly with each other, rather than bubbles from other periods). We have checked that more random perturbations generally do not lead to an overshoot, but elected not to repeat the computations due to their cost and our believe that the long time behaviour is not affected. The four-bubble runs show several oscillations and may have reached a statistically steady-state. The eight bubbles, however, appear to be undergoing unsteady motion on a much longer time scale and we have only computed the evolution until it was clear that the rise Reynolds number was going down again. Although the data here are somewhat limited, they suggest that the larger average rise velocity found for a freely evolving array in two dimensions is also seen in three dimensions.

Figure 11 shows the Reynolds stresses versus time, non-dimensionalized by $d_e g$, for the same runs. The vertical component, $\langle w'w' \rangle$ is shown in figure 11($a$) and the average of the horizontal components, $\frac{1}{2}(\langle u'u' \rangle + \langle v'v' \rangle)$, for the eight-bubble runs, is shown in figure 11($b$). The horizontal component is not shown for the four-bubble runs, since the thinness of the domain limits fluctuation in that direction. Notice that the scale is different for figures 11($a$) and 11($b$). The vertical component shows considerable increase over what is found for a regular array (the single-bubble-in-a-cell case). The horizontal stresses are much smaller than the vertical ones, but still larger than for a regular array. The cross-terms (not shown) should be zero by symmetry for a large number of bubbles, but since the number is small here, these terms fluctuate around zero. Like the rise Reynolds numbers, the Reynolds stresses have not reached a well converged statistically steady-state value at the end of the computations.

Since the computation domain is small, we examine the structure of the bubble distribution by looking only at the immediate vicinity of each bubble. In figure 12 the relative positions of the bubbles in the eight bubble runs are shown for $\alpha = 0.0335$ at twenty one equispaced times and for $\alpha = 0.0654$ at eighteen equispaced times. The reference bubble is located at the origin and each circle denotes another bubble. Since we project the azimuthal component of the position of each bubble onto a single plane, it is important to keep in mind that generally we expect to see a larger

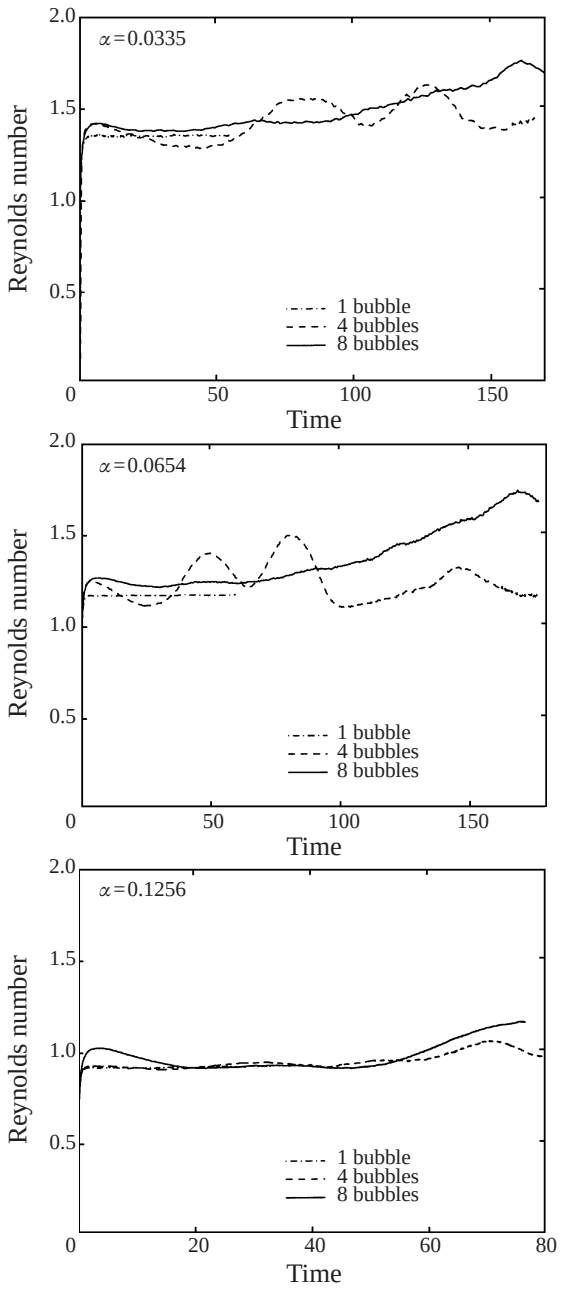


FIGURE 10. The rise Reynolds number versus time for the three-dimensional computations of four and eight bubbles in figure 8, as well as for a single bubble in a cell.

number of bubbles away from the symmetry axis, simply because the volume is larger. The highest volume fraction simulation was run for a relatively short time and is not included here. During the early times, when the bubbles are arranged in an approximately regular array, the lower right-hand corner is crowded by bubbles but as the array breaks up, the relative positions change. The presence of bubbles near the circle that is one diameter away from the origin suggests that actual collisions

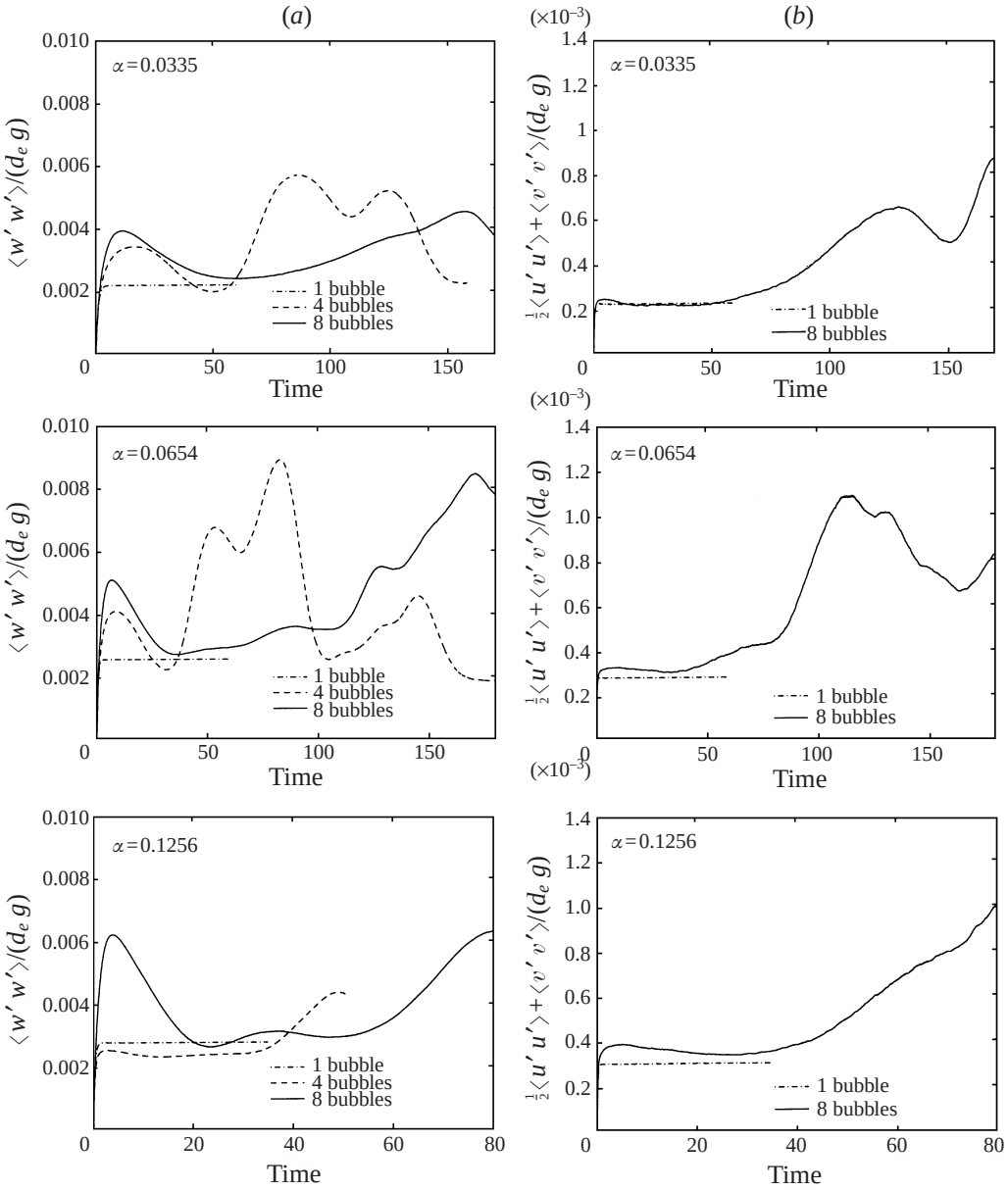


FIGURE 11. (*a*) The vertical Reynolds stresses versus time for the three-dimensional computations in figure 8, as well as for a single bubble in a cell. (*b*) The average of the horizontal Reynolds stresses versus time for the three-dimensional computations of eight bubbles in figure 8(*b*), as well as for a single bubble in a cell.

have taken place. For $\alpha = 0.0335$ this collision point is at approximately 45° but for $\alpha = 0.0654$ it is at approximately 30°. We note that since two bubbles located horizontally with respect to each other repel each other if they are close (Kim, Elghobashi & Sirignano 1993), we do not expect to see any bubbles at $r/d_e = 1$ for $\theta = \pi/2$. Beyond showing that the relative positions change and that some bubbles have collided, it is difficult to infer the actual evolution of the bubble configuration

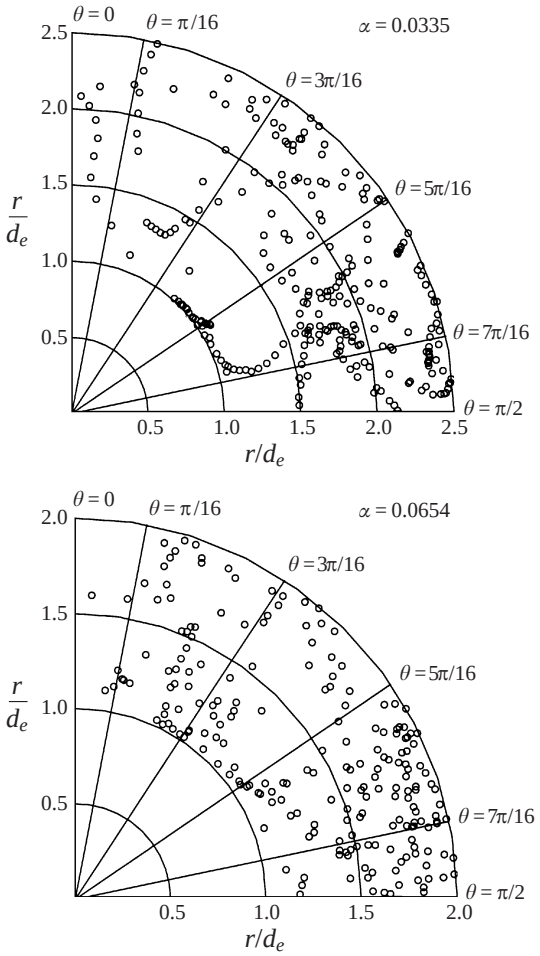


FIGURE 12. The relative locations of bubbles with respect to each other. The data are obtained at 21 equispaced times for $\alpha = 0.0335$ and at 18 equispaced times for $\alpha = 0.0654$.

from these plots. To examine in more detail what is happening very close to the bubbles we have computed the weighted average of $G$ for the interval $1 < r/d_e < 2$ versus time for $\alpha = 0.0335$ (frame *a*) and $1 < r/d_e < 1.5$ for $\alpha = 0.0654$ (frame *b*). The different radial extent of the integration volume is selected to avoid the periodic boundaries. For the fully three-dimensional results, the weighted average is defined by

$$\langle A \rangle = \frac{1}{V} \int G(\boldsymbol{r}) P_2^0(\cos\theta)\, \mathrm{d}v, \tag{3.4}$$

where $\mathrm{d}v$ is a volume element and $P_2^0$ is the second Legendre polynomial (Ladd 1997). We have also computed the average of $G$ for the same region

$$\langle G \rangle = \frac{1}{V} \int G(\boldsymbol{r})\, \mathrm{d}v. \tag{3.5}$$

Figure 13 shows $\langle A \rangle$ and $\langle G \rangle$ versus time for both runs. Due to the large perturbations in the initial conditions, there are bubbles initially located within the shell that we are

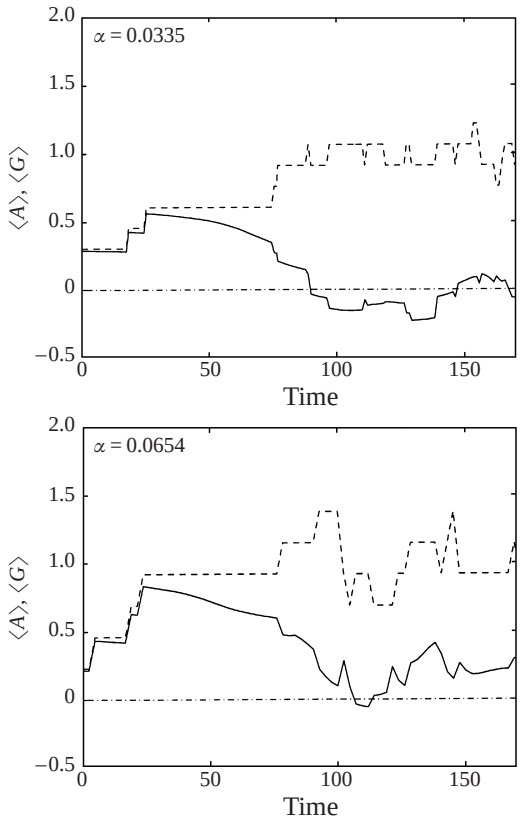


FIGURE 13. The weighted average of $A$ in a shell close to the reference bubble (solid line) and the average $G$ (dashed line) versus time. The size of the shell is selected such that the effect of the periodic boundaries are avoided.

looking at and the graphs do not start from zero. Initially, both graphs start from the same value and rise rapidly as a bubble moves closer to the reference bubble. This shows that the bubbles approach each other along a vertical path. Eventually $\langle A \rangle$ decreases while $\langle G \rangle$ approaches unity. For the higher volume fraction, the evolution is similar, except that the fluctuations are larger since the integration volume is smaller. For the lower volume fraction, the average $\langle A \rangle$ is slightly negative at late times, but since the simulation has not been run for a very long time it is not possible to conclude that the statistically steady-state value of $\langle A \rangle$ will be negative. Both frames in figure 13 suggest, however, that the initial instability of the array takes place by one bubble being drawn into the wake of the one in front, as we observed for the two-dimensional simulations.

### 3.4. *Volume fraction effects*

For homogeneous distributions of bubbles, the dependency of the average rise velocity (or the Reynolds number) on the volume fraction is usually of key interest. We have conducted two-dimensional simulations using sixteen bubbles for both a smaller and a larger computational domain than used in figure 2. Except for the volume fraction, all physical parameters are the same as those in figure 2 and all runs have been carried out until non-dimensional time 160. Initially, the bubbles are distributed in

an irregular way (similar to the runs used to generate the averages in figure 4) and the grids have been selected so the resolutions are comparable to the runs in § 3.1. For each $\alpha$, three runs were done, using different initial positions for the bubbles, and the results averaged over all three runs. In addition to the 16-bubble runs, we have also computed the steady-state motion of a single bubble in a cell for several volume fractions, both for two-dimensional bubbles and fully three-dimensional ones. The result of these computations are shown in figure 14(*a*), along with averages from the three-dimensional runs with four bubbles. The averages are computed over only the second half of the three-dimensional runs to minimize the effect of initial transient. The eight-bubble runs have not reached a sufficiently well defined steady state to justify computing averages. The theoretical results of Sangani (1988) for a cubic array of spherical bubbles in a Stokes flow are also included. The viscosity and density ratio are the same in these simulations, but we do not expect exact agreement since the simulated Reynolds number is not zero.

While the single-bubble-in-a-cell results provide a rigorous reference and allow us to compare with the Stokes flow results of Sangani (1988), the results for the freely evolving array must be interpreted with some care. In particular, since the steady-state averages are likely to depend on the size of the system, the results show the trend of a freely evolving system rather than absolute values. To emphasize this, the data points for the freely evolving systems are connected by a dashed line. As observed earlier, the freely evolving arrays always rise faster than the regular ones. The difference is obviously much larger for the sixteen two-dimensional bubbles than the four three-dimensional ones. While we generally expect weaker interactions among the three-dimensional bubbles, we believe that part of the reason for the small increase is the small number of three-dimensional bubbles. Indeed, the eight-bubble results suggest that the difference may be larger there, once a statistically steady state is reached. Thus, we must conclude that while the present results lend some support to the hypothesis that the dependency on the volume fraction may be well predicted by Sangani's (1988) results for structured arrays (as opposed to random arrays where a linear decrease is predicted, Wacholder 1973; Haber & Hetsroni 1981), the issue awaits the examination of larger systems. The rise velocity of the two-dimensional bubbles increases rapidly as the volume fraction is reduced and while we expect that two-dimensional finite Reynolds number bubbles will approach a finite velocity in the limit of zero volume fraction, we note that predictions for two-dimensional regular arrays in Stokes flow show a logarithmic divergence of the velocity in that limit (Hasimoto 1959).

The Reynolds stresses from the two-dimensional simulations are shown in figure 14(*b*) where we plot

$$\frac{\langle u'u'\rangle}{\alpha\langle W_b\rangle^2} \quad \text{and} \quad \frac{\langle v'v'\rangle}{\alpha\langle W_b\rangle^2}.$$

Here $\langle W_b\rangle$ is the corresponding time-averaged rise velocity of the bubbles. It is clear that scaling the Reynolds stresses in this way makes them approximately independent of the volume fraction. We also see that the stresses for the freely evolving arrays are substantially larger than for the fixed one and that the vertical stresses are much larger than the horizontal ones. The nearly constant value of $\langle u'u'\rangle/\alpha\langle W_b\rangle^2$ is reminiscent of analytical predictions for dilute flows using potential flow around spheres (see, for example, Biesheuvel & van Wijngaarden 1984). Similar results are also easily derived for two-dimensional flow, resulting in $\langle u'u'\rangle = \langle v'v'\rangle = (3/20)\alpha\langle W_b\rangle^2$. The computed value of the horizontal component ($\langle u'u'\rangle$) for a regular array is about 1/3, which is

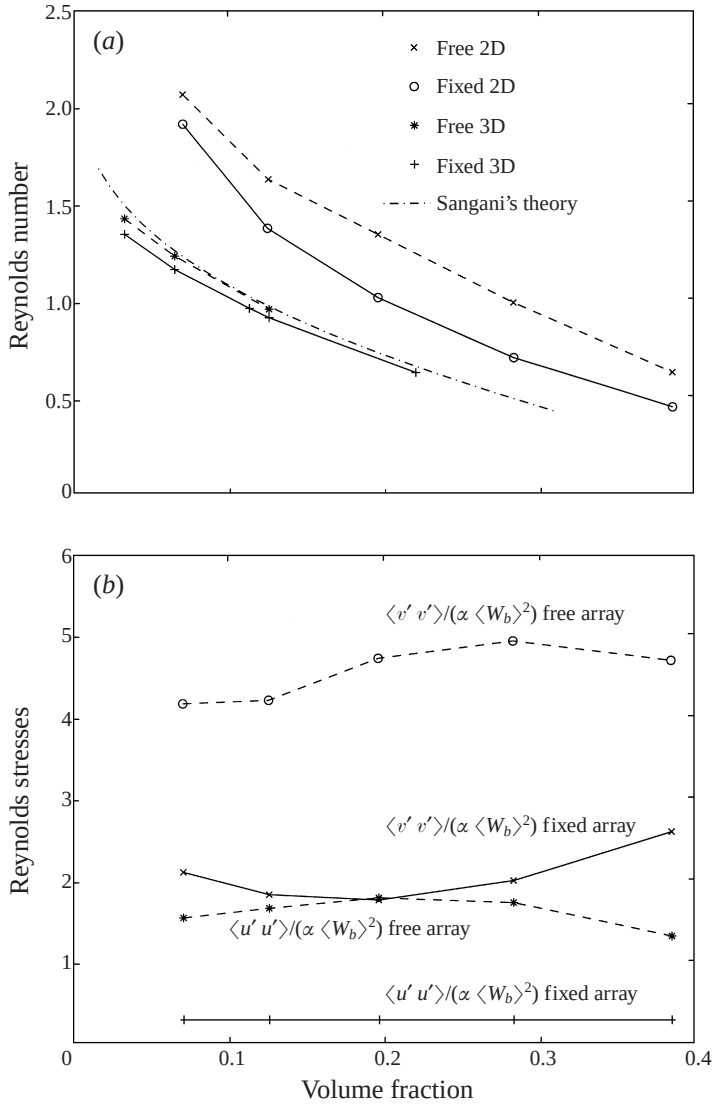


FIGURE 14. (*a*) The effect of the volume fraction on the rise Reynolds number. Results of simulations of both two- and three-dimensional bubbles using both fixed and freely evolving arrays are shown along with the theoretical results of Sangani (1988) for three-dimensional fixed arrays of Stokes flow bubbles. (*b*) The effect of the volume fraction on the Reynolds stresses for two-dimensional simulations of fixed and free arrays. Data points for the free arrays are obtained by ensemble average over the time-averaged results of three simulations at each volume fraction. The Reynolds stresses are scaled by $\alpha\langle W_b\rangle^2$, where $\langle W_b\rangle$ is the corresponding time-averaged rise velocity of the bubbles.

in reasonable agreement with the theory, but the vertical component ($\langle v'v'\rangle$) is not. Since the Reynolds number here is $O(1)$, this is not unexpected. Any averaging of the three-dimensional results is subject to a large uncertainty due to the relatively short time simulated and we have not included any three-dimensional results in figure 14(*b*). The order of magnitude can, however, be seen from the plots in figure 11(*b*). It is clear that the three-dimensional stresses are much smaller, as expected. The vertical

Reynolds stresses are also generally larger than the horizontal ones and this difference is much larger for the three-dimensional bubbles than for the two-dimensional ones. It is also clear that while it may be reasonable to use the results for a regular array to predict the rise Reynolds number of three-dimensional bubbles, a regular array underestimates the Reynolds stresses significantly.

## 4. Conclusions

We have presented direct simulations of the rise of several bubbles in periodic domains. The simulations include fully deformable interface, surface tension, inertia, and viscosity. The Reynolds number is relatively low, but finite. Although most of the simulations are two-dimensional, a few fully three-dimensional results are also included. The results show that regular arrays of both two- and three-dimensional bubbles are unstable and break up relatively quickly. The breakup takes place through the formation of vertically oriented pairs through 'drafting', followed by 'kissing and tumbling'.

Since the two-dimensional computations are much more easily done we have been able to do a large number of such simulations as well as simulating relatively large systems. This, in addition to the relatively strong interaction of two-dimensional bubbles which quickly leads to well converged average quantities, allows us to make fairly well supported observations about these flows. It is clear that a freely evolving array rises considerably faster than a regular array, for example, and although this has an obvious relation to the fact that random arrays of bubbles in Stokes flow rise faster than regular ones, it is also clear that the dynamics of the $O(1)$ Reynolds number flows simulated here are strongly influenced by two-bubble interactions of the 'drafting, kissing, and tumbling' type (Fortes *et al.* 1987). In Stokes flow one must, on the other hand, invoke the influence of a third bubble to account for changes of the relative position of two bubbles. It is also clear that there is only a weak preference for horizontally oriented pairs, in agreement with Stokes flow computations of a large number of spherical solid particles and that – as in Stokes flow – the velocity fluctuations diverge with the size of the system. However, the computations of Esmaeeli & Tryggvason (1996) suggest that this is a finite inertia, two-dimensional effect.

The simulations of the three-dimensional bubbles show that a three-dimensional regular array is unstable and that the breakup mechanism is similar to the two-dimensional one. It also appears that the evolution after breakup may be dominated by two-bubble interactions of the 'drafting, kissing, and tumbling' type. The results for four freely evolving bubbles in a periodic domain show a slight increase in the average rise velocity after breakup and the eight-bubble simulations suggest that this difference increases as the number of bubbles per period is increased. Unfortunately, the size of these computations is limited by computer resources and we have not yet been able to examine what happens as the size of the system is increased.

This work was supported by the National Science Foundation under grants CTS-913214 and CTS-9503208, and the Office of Naval Research under contract N00014-91-J-1084 with Dr E. P. Rood as technical monitor. The computations were done on the computers at the San Diego Supercomputer Center which is sponsored by the NSF, and at the Center for Parallel Computing (CPC) at the University of Michigan. We would like to thank Dr Hal Marshall for his help with using the CPC facilities and Dr John Adams at NCAR for sending us a copy of his latest version of MUDPACK.

## REFERENCES


Adams, J. 1989 MUDPACK: Multigrid FORTRAN software for the efficient solution of linear elliptic partial differential equations. *Appl. Maths Comput.* **34**, 113–146.

Batchelor, G. K. 1972 Sedimentation in a dilute dispersion of spheres. *J. Fluid Mech.* **52**, 245–268.

Batchelor, G. K. 1982 Sedimentation in a dilute polydisperse system of interacting spheres. Part 1. General theory. *J. Fluid Mech.* **119**, 379–408.

Biesheuvel, A. & Wijngaarden, L. van 1984 Two-phase flow equations for a dilute dispersion of gas bubbles in liquid. *J. Fluid Mech.* **148**, 301–318.

Brackbill, J. U., Kothe, D. B. & Zemach, C. 1992 A continuum method for modeling surface tension. *J. Comput. Phys.* **100**, 335–354.

Brady, J. F. & Bossis, G. 1988 Stokesian dynamics. *Ann. Rev. Fluid Mech.* **20**, 111–157.

Caflisch, R. E. & Luke, J. H. C. 1985 Variance in the sedimenting speed of suspensions. *Phys. Fluids* **28**, 759–760.

Chahine, G. L. 1994 Strong interactions bubble/bubble and bubble/flow. In *IUTAM* conference on bubble dynamics and interfacial phenomena (ed. J. R. Blake). Kluwer.

Clift, R., Grace, J. R. & Weber, M. E. 1978 *Bubbles, Drops, and Particles.* Academic.

Davis, R. H. & Acrivos, A. 1985 Sedimentation of noncolloidal particles at low Reynolds numbers. *Ann. Rev. Fluid Mech.* **17**, 91–118.

Drew, D. A. 1983 Mathematical modeling of two-phase flow. *Ann. Rev. Fluid Mech.* **15**, 261–291.

Drew, D. A. & Lahey, R. T. Jr. 1993 Analytical modeling of multiphase flow. In *Particulate Two-Phase Flow* (ed. M. C. Roco), pp. 509–566. Butterworth.

Elghobashi, S. & Truesdell, G. C. 1993 On the two-way interaction between homogeneous turbulence and dispersed solid particles. I: Turbulence modification. *Phys. Fluids* A **15**, 1790–1801.

Esmaeeli, A. 1995 Numerical simulations of bubbly flows. PhD Thesis, The University of Michigan.

Esmaeeli, A. & Tryggvason, G. 1996 An inverse energy cascade in two-dimensional, low Reynolds number bubbly flows. *J. Fluid Mech.* **314**, 315–330.

Esmaeeli, A. & Tryggvason, G. 1999 Direct numerical simulations of bubbly flows. Part 2. Moderate Reynolds number arrays. *J. Fluid Mech.* (to appear).

Feng, J., Hu, H. H. & Joseph, D. D. 1994 Direct simulation of initial value problems for the motion of solid bodies in a Newtonian fluid. Part 1. Sedimentation. *J. Fluid Mech.* **261**, 95–134.

Feng, J., Hu, H. H. & Joseph, D. D. 1995 Direct simulation of initial value problems for the motion of solid bodies in a Newtonian fluid. Part 2. Couette and Poiseuille flows. *J. Fluid Mech.* **277**, 271–301.

Fortes, A., Joseph, D. D. & Lundgren, T. 1987 Nonlinear mechanics of fluidization of beds of spherical particles. *J. Fluid Mech.* **177**, 467–483.

Glimm, J. 1991 Nonlinear and stochastic phenomena: The grand challenge for partial differential equations. *SIAM Rev.* **33**, 625–643.

Haber, S. & Hetsroni, G. 1981 Sedimentation in dilute dispersion of small drops of various sizes. *J. Colloid Interface Sci.* **79**, 56–74.

Happel, J. & Brenner, H. 1965 *Low Reynolds Number Hydrodynamics.* Prentice-Hall.

Harlow, F. H. & Welch, J. E. 1965 Numerical calculation of time-dependent viscous incompressible flow of fluid with free surfaces. *Phys. Fluids* **8**, 2182–2189.

Hasimoto, H. 1959 On the periodic fundamental solution of the Stokes equations and their application to viscous flow past a cubic array of spheres. *J. Fluid Mech.* **5**, 317–328.

Hirt, C. W. & Nichols, B. D. 1981 Volume of fluid (VOF) method for the dynamics of free boundaries. *J. Comput. Phys.* **39**, 201–226.

Hu, H. H. 1996 Direct simulation of flows of liquid-solid mixtures. *Intl J. Multiphase Flow* **22**, 335–352.

Ishii, M. 1987 Two-fluid model for two-phase flow. In *Proc. 2nd Intl Workshop on Two-Phase Flow Fundamentals*, RPI, March 16–20.

Ishii, M. & Zuber, N. 1979 Drag coefficient and relative velocity in bubbly, droplet or particulate flows. *AIChE J.* **25**, 843–855.

Jan, Y.-J. 1993 Computational studies of bubble dynamics. PhD Thesis, The University of Michigan, Ann Arbor.

Johnson, A. A. & Tezduyar, T. E. 1997 3D simulation of fluid-particle interactions with the number of particles reaching 100. *Comput. Methods Appl. Mech. Engng* **145**, 301–321.

Kennedy, M. R., Pozrikidis, C. & Skalak, R. 1994 Motion and deformation of liquid drops, and the rheology of dilute emulsions in simple shear flows. *Computers Fluids* **23**, 251–278.

Kim, I., Elghobashi, S. & Sirignano, W. A. 1993 Three-dimensional flow over two spheres placed side by side. *J. Fluid Mech.* **246**, 465–488.

Koch, D. L. 1993 Hydrodynamic diffusion in dilute sedimenting suspensions at moderate Reynolds numbers. *Phys. Fluids* A **5**, 1141–1155.

Koch, D. L. & Shaqfeh, E. S. G. 1991 Screening in sedimenting suspensions. *J. Fluid Mech.* **224**, 275–303.

Ladd, A. J. C 1993 Dynamical simulations of sedimenting spheres. *Phys. Fluids* A **5**, 299–310.

Ladd, A. J. C. 1997 Sedimentation of homogeneous suspensions of non-Brownian spheres. *Phys. Fluids* **9**, 491–499.

Lafaurie, B., Nardone, C., Scardovelli, R., Zaleski, S. & Zanetti, G. 1994 Modeling merging and fragmentation in multiphase flows with SURFER. *J. Comput. Phys.* **113**, 134–147.

Lamb, H. 1932 *Hydrodynamics*, Dover.

Lance, M. & Bataille, J. 1991 Turbulence in the liquid phase of a uniform bubbly air-water flow. *J. Fluid Mech.* **222**, 95–118.

Loewenberg, M. & Hinch, E. J. 1996 Numerical simulation of a concentrated emulsion in shear flow. *J. Fluid Mech.* **321**, 395–419.

Magnaudet, J. J. M. 1997 The force acting on bubbles and rigid particles. *ASME FED* Summer Meeting, June 22–26 (FEDSM97-3522).

Manga, M. & Stone, H. A. 1993 Buoyancy-driven interactions between deformable drops at low Reynolds numbers. *J. Fluid Mech.* **256**, 647–683.

Miyata, H. 1996 Time-marching cfd simulation for moving boundary problems. 21st symposium on naval hydrodynamics, June 24–28, Trondheim, Norway, pp. 1–21.

Mizukami, M., Parthasarathy, R. N. & Faeth, G. M. 1992 Particle-generated turbulence in homogeneous dilute dispersed flows. *Intl J. Multiphase Flow* **18**, 397–412.

Nicolai, H. & Guazzelli, E. 1995 Effect of vessel size on the hydrodynamics diffusion of sedimenting spheres. *Phys. Fluids* **7**, 3–5.

Revay, J. M. & Higdon, J. J. L. 1992 Numerical simulations of polydisperse sedimentation: equal-sized spheres. *J. Fluid Mech.* **243**, 15–32.

Richardson, J. F. & Zaki, W. N. 1954 Sedimentation and fluidization. Part I. *Trans. Inst. Chem. Engrs* **32**, 35–53.

Ryskin, G. & Leal, L. G. 1984 Numerical solution of free-boundary problems in fluid mechanics. Part 2. Buoyancy-driven motion of a gas bubble through a quiescent liquid. *J. Fluid Mech.* **148**, 19–35.

Sangani, A. S. 1988 Sedimentation in ordered emulsions of drops at low Reynolds number. *Z. Angew. Maths Phys.* **38**, 542–555.

Sangani, A. S. & Acrivos, A. 1982*a* Slow flow past periodic arrays of cylinders with application to heat Transfer. *Intl J. Multiphase Flow* **8**, 193–206.

Sangani, A. S. & Acrivos, A. 1982*b* Slow flow through a periodic arrays of spheres. *Intl J. Multiphase Flow* **8**, 343–360.

Sangani, A. S. & Acrivos, A. 1983 Creeping flow through cubic arrays of spherical bubbles. *Intl J. Multiphase Flow* **9**, 181–185.

Sangani, A. S. & Didwania, A. K. 1993 Dynamic simulations of flows of bubbly liquids at large Reynolds numbers. *J. Fluid Mech.* **250**, 307–337.

Singh, P. & Joseph, D. D. 1995 Dynamics of fluidized suspension of spheres of finite size. *Intl J. Multiphase Flow* **21**, 1–26.

Smereka, P. 1993 On the motion of bubbles in a periodic box. *J. Fluid Mech.* **254**, 79–112.

Sussman, M., Smereka, P. & Osher, S. 1994 A level set approach for computing solutions to incompressible two-phase flows. *J. Comput. Phys.* **114**, 146–159.

Takagi, S. & Matsumoto, Y. 1994 Three-dimensional deformation of a rising bubble. *Proc. German-Japanese Symp. on Multiphase Flow KfK 5389*, p. 499.

Tomiyama, A., Sou, A., Žun, I. & Sakaguchi, T. 1994 Three-dimensional detailed numerical

simulation of bubbly upflow in a vertical square duct. *Proc. German-Japanese Symp. on Multiphase Flow KfK 5389*, p. 487.

Tryggvason, G. & Unverdi, S. O. 1990 Computations of three-dimensional Rayleigh–Taylor instability. *Phys. Fluids* A **2**, 656–659.

Unverdi, S. O. & Tryggvason, G. 1992*a* A front-tracking method for viscous, incompressible, multi-fluid flows. *J. Comput. Phys.* **100**, 25–37.

Unverdi, S. O. & Tryggvason, G. 1992*b* Computations of multi-fluid flows. *Physica* D **60**, 70–83.

Wacholder, E. 1973 Sedimentation in a dilute emulsion. *Chem. Engng Sci.* **28**, 1447–1453.

Wang, L. P. & Maxey, M. 1993 Settling velocity and concentration distribution of heavy particles in homogeneous isotropic turbulence. *J. Fluid Mech.* **256**, 27–68.

Weatherburn, C. E. 1927 *Differential Geometry of Three Dimensions*, Vol. 1. Cambridge University Press.

Zhang, D. Z. & Prosperetti, A. 1994 Averaged equations for inviscid disperse two-phase flow. *J. Fluid Mech.* **267**, 185–219.

Zhou, H. & Pozrikidis, C. 1993 The flow of ordered and random suspensions of two-dimensional drops in a channel. *J. Fluid Mech.* **255**, 103–127.

Zhou, H. & Pozrikidis, C. 1994 Pressure-driven flow of suspensions of liquid drops. *Phys. Fluids* **6**, 80–94.

Zick, A. A. & Homsy, G. M. 1982 Stokes flow through periodic arrays of spheres. *J. Fluid Mech.* **115**, 13–26.

Zuber, N. 1964 On the dispersed two-phase flow in the laminar flow regime. *Chem. Engng Sci.* **19**, 897–917.